Chapter 17

Electrical Resistance Tomography—Theory and Practice

William Daily[1], *Abelardo Ramirez*[1], *Andrew Binley*[2], *and Douglas LaBrecque*[3]

Historical Development

During the last two decades, the United States government has emphasized the environmental remediation of the subsurface contamination which is a legacy of the previous decades of the U.S.-Soviet Cold War. This legacy includes radioactive, chemical, and biological contamination at thousands of sites across the country. The cleanup was, and remains, costly, with many problems solvable only with the development of new technologies. The early development of electrical resistance tomography (ERT) was mainly in response to the need for new technologies to generate high-resolution images of the shallow subsurface. Also, much of the early use of ERT was site characterization or process monitoring for soil and groundwater cleanup.

ERT is a method that calculates the subsurface distribution of electrical resistivity from a large number of resistance measurements made from electrodes placed in an arbitrary geometric pattern. For in-situ applications, ERT uses electrodes on the ground surface or in boreholes. ERT may also be utilized in a similar manner for imaging biomedical targets, rock or soil core, and block structures. The method has contributed to the fields of hydrogeology, soil science, oil reservoir management, engineering investigations, and glaciology. Developments in instrumentation and data inversion algorithms have led to applications of 3D imaging of time-dependent processes and, more recently, extensions to incorporate induced-polarization effects.

This chapter contains several ERT case studies of subsurface clean up, site characterization and process monitoring, applied at a range of scales and in a range of geologic environments. We will also outline the historical development of ERT and present an overview of data acquisition and data processing techniques. Our aim is to provide a review of the method, highlighting strengths and weaknesses, in addition to including theoretical developments and important practical issues.

In the early 1900s Conrad and Marcel Schlumberger pioneered exploration of the subsurface using galvanic currents (Schlumberger, 1920). At the time, seismic methods were already a popular method for probing the subsurface, especially on a scale of hundreds to thousands of meters, and were used extensively in oil and gas exploration. The new electrical resistance method was quickly found to be useful for sulfide mineral exploration. It also became apparent that this method was going to be an important tool for the geophysicist because of its value in the identification of other rocks and minerals and its sensitivity to subsurface liquids.

From the 1920s until the 1970s, electrical prospecting was developed and applied to geophysical problems, but with severe limitations in both the measurement equipment and interpretation strategies. Even into the 1970s, one of the most popular engineering resistivity systems consisted of little more than a box of batteries, a galvanometer and a mechanically balanced Wheatstone bridge. Interpretation consisted largely of comparing field plots of apparent resistivity to curves derived from simple analytic models or scale model studies (e.g., Keller and Frischkneckt, 1966). To apply these crude interpretation techniques, field measurements had to be taken using one of a few standard configurations or arrays. Data were generally collected as soundings using the Schlumberger or Wenner arrays or using the dipole-dipole or pole-dipole array. Data were sometimes displayed in a two-dimensional array using a simple but useful scheme called a *pseudosection* (see Marshall and Madden, 1959).

In the 1970s things began to change rapidly. First, by the late 1970s virtually all research institutes and most large corporations had access to increasingly powerful mainframe computers. Second, relatively inexpensive, low-power microprocessors were becoming widely available. Along with other advances in electronics, microprocessors made sophisticated data acquisitions systems practical. The advent of high-speed computers made practical new modeling methods developed by Coggon (1971), Hohmann (1975), Dey and Morrison (1979 a,b) and were used either to enhance or supplement older model catalogs.

---

[1] Lawrence Livermore National Laboratory, Livermore, CA 94550. William Daily E-mail: daily1@llnl.gov. Abelardo Ramirez E-mail: ramirez3@llnl.gov.

[2] Lancaster University, Lancaster, LA1 4YQ, UK. E-mail: A.Binley@lancaster.ac.uk

[3] Multi-phase Technologies, LLC, Sparks, NV 89436. E-mail: Dlabrec887@yahoo.com.

https://doi.org/10.1190/1.9781560801719.ch17

During this same period, initial work began on applying inverse methods to sounding data and later to two-dimensional model fitting (Tripp et al. 1984).

During the 1970s, tomographic reconstruction of cross-sectional data was first applied in medical diagnostics (Hounsfield, 1973) and numerical calculations on high-speed digital computers made computed tomography practical. This initial work was for reconstruction of X-ray attenuation using the concept of back projection of X-ray transmission intensity. However, it was shown that a similar back projection algorithm could be used to reconstruct two dimensional electrical resistivity for medical imaging (see Lytle and Dines, 1978; Barber et al., 1983). Related methods were also developed for increased sensitivity (see Gisser et al., 1987) and for three-dimensional analysis (Wexler et al., 1985; Goble and Isaacson, 1989). A good review of the early work in medical electrical tomography is given by Webster (1990).

Concepts borrowed from the medical use of computed tomography soon migrated to geophysics (Lager and Lytle, 1977; Dines and Lytle, 1979). X-rays, practical for probing density structure of humans, were replaced by radio frequency energy for geophysical imaging. This change made geophysical tomography practical for probing electromagnetic properties of soils and rocks on a much larger scale than that needed for medical diagnostics. As a result of that early work, cross-borehole GPR (ground-penetrating radar), as it is known, remains today a useful geophysical imaging tool (e.g., Daily and Lytle, 1983; Hubbard et al., 1997; Binley et al., 2001a).

This work also inspired the development of seismic tomography (Aki et al., 1976; Anderson and Dziewonski, 1984) and later, low-frequency electromagnetic tomography (Wilt et al., 1995). The first significant work on ERT began in the 1980s. Notable work at this time was the 2D modeling of Shima and Sakayama (1987) and Shima (1990) based on the alpha center method and inverted using back projection methods and finite element modeling of Sasaki (1989, 1994). Lytle and Dines (1978) and Daily and Owen (1991) borrowed some of the methods of electrical tomography being developed for medical diagnostics (Yorkey et al., 1987) and showed that geophysical electrostatic (or galvanic) electrical imaging was possible.

Electrical resistance tomography, as it became known, was a marriage of traditional electrical probing as introduced by the Schlumberger brothers and the new data inversion methods of tomography. Tomographic inversion added important new capabilities because it provided more general, quantitative, and rigorous spatial imaging of geophysical electrical resistance data than was the earlier pseudosection or curve fitting methods.

The initial application of geophysical ERT was to image laboratory core samples under test (Daily et al., 1987). Practical field scale use of ERT was delayed by the need for suitable measurement and test equipment. ERT requires the same four electrode resistance measurement used by the Schlumberger brothers (two electrodes to inject current and two other electrodes to measure the resulting potential), however, tomography requires addressing tens or hundreds of electrodes and making hundreds or thousands of such measurements. Clearly, the available manual measurement systems that were designed for one, or perhaps a few measurements at a time, were not practical for ERT. High-speed, automated systems were needed.

The first system for practical application of geophysical ERT was constructed at Lawrence Livermore National Laboratory by two of the authors (Daily and Ramirez) in 1989. This system combined a commercial geophysical resistivity instrument (capable of producing the switched DC source and making the synchronous voltage measurement on four electrodes), a commercial multiplexer capable of connecting the resistivity instrument to 20 electrodes, and a computer to control the process and archive the data (Ramirez et al., 1993). The system was much faster than manual data acquisition and eliminated electrode connection and data transcription errors. Today, measurement systems are commercially available that are 10 to 20 times faster (up to a few thousand measurements per hour) and that can simultaneously address hundreds of electrodes (Shore, 1992; Daily et al., 1996).

Following the development of robust inversion routines and suitable data acquisition systems, ERT was applied to a wide range of environmental and engineering problems including the monitoring of vadose zone water movement (Daily et al., 1992; Schima et al., 1996), steam injection (Ramirez et al., 1993) and air sparging (Schima et al., 1996, Lundeguard and LaBrecque, 1995).

Data Acquisition Systems

In ERT, four electrodes are used to make the measurement to minimize the effect of contact resistance (Brown and Seagar, 1985; Yorkey et al., 1985) at the interface between the soil pore water and the electrode. A known current is forced through two electrodes and the potential difference is measured on the other two electrodes. Figure 1 schematically represents how this might be done for a cross-borehole case. In the frequency domain, the transmitted current $I(\omega)$ and measured voltage $V(\omega)$ are related by Ohm's law to the impedance $Z(\omega)$, where these quantities are complex to account for both magnitude (resistance) and phase (polarization). In the time domain, the current and voltage are related by a magnitude and chargability (see Telford, et al., 1976 and Kemna, 2000). The impedance is then often represented as a quotient $\rho_a(\omega)/G$ of the complex apparent resistivity and a geometrical factor, which accounts for the arrangement of the electrodes. The

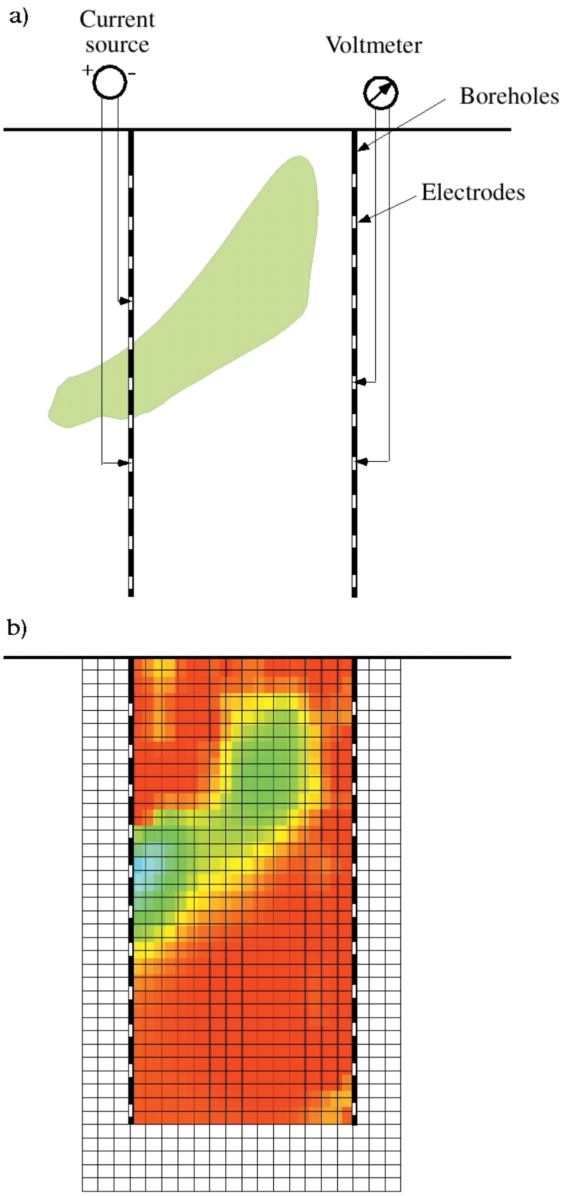

Figure 1. Schematic of ERT measurement and image reconstruction. (a) Electrode array and example 4 electrode measurement for cross-borehole ERT. Electrodes can be along the surface, in boreholes, or both. (b) Typical finite element mesh used in data processing.

imaginary part of the impedance accounts for the electrode or membrane polarization induced in porous media even at these low frequencies (e.g., 1 Hz). Marshall and Madden (1959) provide a good review of the various mechanisms responsible for induced polarization.

To obtain the large number of independent impedance measurements necessary for tomographic inversion, all possible linearly independent combinations from an array of electrodes are used. For *n* electrodes there are *n*(*n* – 1)/2 such combinations (Yorkey et al., 1987). These combinations can be obtained using various strategies. One popular approach for field measurements is a pole-pole measurement scheme where one remote electrode (at "infinity") is used as one current pole and another remote electrode is used as a voltage reference pole. The two other poles, one for current and one for potential, are used in all the combinations possible in the array. For *n* electrodes in the array (not including the remote electrodes) there are *n*(*n* – 1) transfer resistance measurements. Only half of these are linearly independent, because when the current source and voltage electrodes are interchanged, the measurements are reciprocal (defined below) and, except for nonlinear effects, should be identical. Another approach is the dipole-dipole measurement scheme, where two electrodes are used to inject current and two electrodes are used to measure a differential potential. Again, all independent combinations are usually taken and half of these are reciprocal.

A very large number of other measurement schemes is possible, some of which have been found useful (i.e., Schlumberger and Wenner arrays). There has been some discussion about the relative merits of these sampling schemes (see Zhou and Greenhalgh, 1997) regarding sensitivity patterns for various electrode configurations. Recently, Bing and Greenhalgh (2000) have studied several sampling schemes by comparing inversions of synthetic data. They conclude that pole-pole and some forms of pole-dipole schemes are suitable for cross-borehole ERT. Such synthetic studies are very valuable; however, we believe that the concept of a "universal" measurement scheme for ERT is probably not achievable. In any case, it is critical that real measurement error be considered in any analysis. Measurement errors are generally not random and data inversions are strongly dependent on them, as will be shown later. Furthermore, measurement errors will be strongly dependent on the environment to which ERT is applied, and sensitivity and resolution will depend on the resistivity structure itself. At this time we are certain of two things:

1) It is important to sample the electrode array to obtain all the linearly independent data. This has been achieved when any additional measurement can be constructed by linear superposition of measurements already taken.
2) It is important to sample the array to obtain each measurement and its reciprocal. A reciprocal measurement is made by interchanging the electrode pairs used for voltage measurement with the electrode pair used for current injection. The transfer impedance for these two cases will be identical if the system is responding linearly (i.e., according to Ohm's law) and there is no measurement error. Therefore, a comparison of a measured resistance in a reciprocal provides an estimate of data error that is a more reliable indicator of error than repeatability. The importance of having a good estimate of this error cannot be overstated.

> LaBrecque et al. (1996) showed that, because of the statistical nature of the more sophisticated and reliable inversion algorithms, it is better to have higher data error but know the character of that error than have a lower data error and not know the magnitude of the error. The reason for this will be apparent from the discussion of inversion methods that will appear later.

ERT electrodes may be on the surface, in boreholes, or both. Early work was cross borehole—sampling electrodes were placed into two or more boreholes. Later, other modalities quickly evolved including single borehole, borehole to surface, surface only, and all combinations of these possibilities. Possible sampling combinations are usually limited by the cost of electrode installation and the flexibility of numerical modeling codes. However, sometimes the sampling scheme is limited by physical constraints such as surface conditions (e.g., buildings, steel structures) ruling out remote electrodes or asphalt ruling out surface electrodes.

The basic components of any acquisition system are transmitter or current source; receiver which measures the resulting electrode potentials; multiplexer for quickly and automatically connecting the electrodes to the transmitter and receiver; and a computer for system control and data archival. A block diagram of a typical system is shown in Figure 2. Details of one commercially available system can be found in Ramirez et al. (1999).

Data collection rates are determined by the number of channels (detectors) in the receiving unit, source frequency, gain ranging by detectors, and waveform stacking requirements. Under typical conditions for a system of 16 channels at 4 Hz and stacking for 1 s, it is possible to acquire data with about 1% error in the magnitude (as determined by comparing reciprocal measurements) at a rate of about 2000 measurements per hour. This data rate can be increased by premeasuring the analog amplifier gains for each measurement and using these gain settings instead of allowing the system to determine them before each measurement. Using prerecorded gains, the data rate increases to about 3000 measurements per hour. Of course, as the current injection frequency increases gain setting and staking require less time and data rates will be higher.

Data accuracy is usually defined as "the conformity of an indicated value to an accepted standard value, or true value" (Considine, 1983). As one measure of system accuracy, we use a simple system calibration against a standard resistor. One channel is used to measure the current through a standard resistor (with a NIST pedigree), while another channel is used to measure the resulting potential drop. Calibration accuracy is typically better than 1%. We routinely use this procedure as a measurement system check.

Within the past few years, several data acquisition systems have become available on the commercial market, and as could be expected, there is a strong correlation between price and capabilities. The more expensive systems are capable of addressing many electrodes (30 and more), making many (16 and more) simultaneous voltage measurements, and offer a wide dynamic range. The first two of these capabilities translate into higher data acquisition rates, which can be an important consideration when thousands or even tens of thousands of measurements are required to monitor dynamic processes such as a steam flood. The wide dynamic range offered by more expensive systems permits a wider range of ERT applications in a wide variety of geologic environments. This is particularly important for borehole deployed electrodes that may suffer from high contact resistances and transfer resistance values ranging over several orders of magnitude.

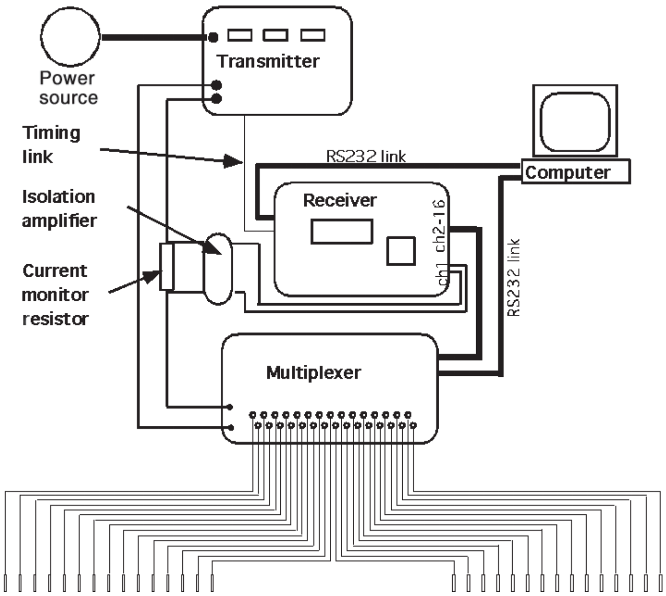

Figure 2. Schematic of a typical ERT data acquisition system.

One important design difference between various systems is the way in which the source and detectors are multiplexed to the electrodes. Some systems have "active" electrodes wherein the switching is done in a small electronics package at each electrode location. This arrangement requires only four wires to run between the electrodes along the array—two for the current source and two for differential voltage measurement. Active electrodes are easy to install, especially in surface arrays, although they are expensive when used (permanently placed) in boreholes. Other systems make use of a "dumb" electrode wherein the switching is done in a switching location away from the electrode, and a single wire is needed to connect each electrode to that set of switches (multiplexer). This arrangement usually requires many long wires and is therefore more difficult to install. However, because the electrodes are usually inexpensive pieces of metal (e.g. stainless steel, copper, or iron) and because copper wire is relatively inexpensive, this arrangement is usually chosen for downhole use.

Although older systems only measured the amplitude of voltage divided by current (which we will refer to as the transfer resistance), most systems now measure some form of induced polarization as well. Induced polarization measures the time or frequency dependence of resistivity. Historically, geophysicists have used three different quantities for induced polarization: percent frequency effect, phase, and chargeability (Telford et al., 1976). Percent frequency effect compares the independent measurements of the amplitude of resistivity at two different frequencies. Such measurements are generally considered obsolete as phase and chargeability measurements can be made more quickly and accurately.

Frequency-domain systems are designed specifically to measure phase and amplitude of a single frequency f_0, or series of harmonic frequencies ($1\,f_0$, $3\,f_0$, $5f_0$ …). Alternatively, a time-domain waveform can be discretized and Fourier transformed to provide the phase and amplitude for a range of frequency spectra (see Kemna, 2000). Time-domain systems, measure the voltage while the transmitter is turned on and that voltage is used to calculate the resistivity amplitude. Chargeability is obtained after the transmitted current is turned off by measuring the integral of the voltage decay waveform.

Data Processing—Forward and Inverse Algorithms

In order to calculate a resistivity image from ERT data, it is necessary to carry out an inversion procedure that produces a model (that is, a spatially varying distribution of resistivity) that gives an "acceptable" fit to the data and satisfies any other prescribed constraints. Unfortunately, an acceptable fit may be viewed as subjective, as we shall see later. We may start from the view that an objective function defines how well the model would reproduce the field measurements subject to a level of uncertainty in the data. Thus, the numerical procedure requires three elements: a forward model that computes transfer impedance (or resistance for the DC problem) given a 2D or 3D distribution of resistivity; an objective function that states the model fitting criteria that will be adopted; and a search algorithm which determines the way in which the "optimum" resistivity model is found.

We show here details of these elements for the general 3D complex resistivity case, highlighting, where appropriate, how 2D and or DC resistivity implementation may differ. The approach is described using conductivity (resistivity inverse) as the variable of interest in order to simplify notation and remain consistent with examples in the literature. In the following, the symbol * is used to indicate complex variables, for example, σ^* is the complex conductivity and σ is the real value (as determined in DC ERT).

Forward model

Assuming a 3D distribution of isotropic, complex conductivity $\sigma^*(x,y,z)$, the forward model may be defined by the equation for point source current I as:

$$\frac{\partial}{\partial x}\left(\sigma^*\frac{\partial V^*}{\partial x}\right)+\frac{\partial}{\partial y}\left(\sigma^*\frac{\partial V^*}{\partial y}\right)+\frac{\partial}{\partial z}\left(\sigma^*\frac{\partial V^*}{\partial z}\right)=-I\,\delta(x)\,\delta(y)\,\delta(z), \tag{1}$$

subject to boundary conditions:

$$\sigma^*\frac{\partial v^*}{\partial n}+\beta^* V^*=0, \tag{2}$$

where v^* is the complex potential, δ is the Dirac delta function, n is the outward normal, and β^* defines the boundary type. In most cases, we have Neumann boundary conditions as the surface ($\beta^* = 0$) and mixed boundary conditions (β^* finite and nonzero) along the remaining boundaries. In this case, equation (2) defines a mixed boundary condition also called a *nonreflecting boundary*. The purpose of mixed boundary conditions is to remove the necessity to model current flow at significant distances from the zone of interest when approximating a semi-infinite region (Dey and Morrison, 1979a).

Simplification to 2D conductivity distributions requires Fourier transformation in order to account for 3D current flow. The model may be expressed as

$$\frac{\partial}{\partial x}\left(\sigma^*\frac{\partial v^*}{\partial x}\right)+\frac{\partial}{\partial z}\left(\sigma^*\frac{\partial v^*}{\partial z}\right)-\lambda^2\sigma^* v^*=-I\,\delta(x)\delta(z), \tag{3}$$

where λ is the Fourier-transform variable corresponding to the strike direction y, v^* is the complex potential in the Fourier domain. Adopting this approach, an inverse Fourier transformation must be applied to the solution of equation (3) to recover potentials V^* (see for example, LaBrecque et al., 1996; Kemna, 2000).

Analytical solutions to equation (1) or (3) are not available for arbitrary conductivity distributions, and thus numerical solutions are required. Typically, finite-element (FE) or finite-difference (FD) approaches are used. In both cases the region is discretized into discrete points (nodes) and an approximate solution is determined at these points. Variation in conductivity is achieved by assigning values on an element by element (FE) or cell by cell (FD) basis. By positioning nodes at electrode locations, it is possible to compute transfer impedances for arbitrary measurement configurations.

The FE approach allows flexibility in discretization and thus may be preferred for irregular electrode positioning. In addition, treatment of irregular topography and other boundary features is easily achieved in comparison to the FD method. The FD approach, however, is by far simpler in operation and computationally more efficient for regular geometry. Sasaki (1994) illustrates the flexibility of the FE approach for surface electrode DC resistivity modeling in contrast to the FD method presented by Dey and Morrison (1979a,b). Kemna (2000) provides a thorough analysis of how the FE method may be applied to 2D complex resistivity models.

Computational efficiency of the forward model is essential for large (> 10^5 nodes) 3D problems. For such large problems, the solution of the discretized equations must be achieved through iterative methods, the conjugate gradient method being the commonest approach. For complex resistivity modeling, variants of the conjugate-method are available (see for example, Hestenes, 1980). For the DC case, Bing and Greenhalgh (2001) compare different finite element discretization methods for 3D forward modeling and provide a useful comparison of matrix solution techniques. Attempts have been made to improve modeling of singularities in the forward model created at the current electrode locations. Lowry et al. (1989) offers an approach to account for such effects, while Zhao and Yedlin (1996) suggest a refined solution. These methods have been incorporated into forward modeling codes, but they have not seen widespread use in inverse solutions. Although these methods improve the accuracy of the solution for simple cases, there is some question as to their accuracy in arbitrary 3D models particularly when source or receiving electrodes lie on or near the edges or corners of 3D regions of anomalous conductivity or when the source and receivers lie in different regions of high-conductivity contrast.

Inverse model

For the inverse model the region is discretized into parameters, denoted here as vector $\mathbf{m}^*$. These may be assigned to blocks of elements, or they may be assigned to individual elements (or cells). Because of the large possible range in earth conductivity, log-transformed conductivity is normally used as the inversion parameter:

$$m_j^* = ln\sigma_j^* \quad (j = 1, \ldots, M), \tag{4}$$

where M is the number of parameter blocks.

The inverse model attempts to determine the "best" set of parameters $\mathbf{m}^*$ that match the data using the forward model [equation (1) or (3)] to compute the transfer impedances for the given measurement configurations. If we denote the transfer impedances as Z_i^*, $i = 1, \ldots, N$, where N is the number of measurements, then a log transformed data vector $\mathbf{d}^*$ may be used, where

$$d_i^* = -\ln(Z_i^*) \quad (i = 1, \ldots, N). \tag{5}$$

The log transformation in equation (5) is used because of the wide range in measured impedances for arbitrary electrode configurations. Note that use of the log transformation in equation (5) requires the polarity of measured and modeled impedances to be identical, which is not necessarily guaranteed for the general ERT problem. Consequently, if such an approach is used, then those measurements not satisfying this criteria must not be included in the inversion process, or be temporarily neglected in the inversion until they satisfy the criteria. Because of the extra bookkeeping required, the log transformation of data in equation (5) is often not used.

The L_2 measure of data misfit may be used as an objective function which the inverse solution seeks to minimize. This is expressed as

$$\Psi_d(\mathbf{m}^*) = \left\| \mathbf{W}_{\mathrm{d}}^* \left[\mathbf{d}^* - \mathbf{f}^*(\mathbf{m}^*) \right] \right\|^2, \tag{6}$$

where $\mathbf{f}^*$ is the forward model operator and $\mathbf{W}_{\mathrm{d}}^*$, is a complex data weighting matrix.

Assuming uncorrelated data errors, the data weighting matrix may be expressed in terms of the data errors ε_i^* ($i = 1, \ldots, N$) as:

$$\mathbf{W}_{\mathrm{d}}^* = \mathrm{diag}\left(1/\varepsilon_1^*, \ldots, 1/\varepsilon_N^* \right). \tag{7}$$

Unfortunately due to the ill-posedness of the inverse solution for ERT, using the objective function in equation (6) usually results in unstable solutions. To constrain the inversion, regularization is normally adopted. To achieve this, it is necessary to modify the objective function to include stabilizing terms that constrain the parameter search. In general terms, this composite objective function may be written as

$$\Psi(\mathbf{m}^*) = \Psi_d(\mathbf{m}^*) + \Psi_m(\mathbf{m}^*), \tag{8}$$

where $\Psi_m(\mathbf{m}^*)$ is a measure of the model misfit. It can contain a measure of "roughness," that is, how variable adjacent parameter values vary, and also a measure of how much the parameters differ from some specified model, such that deviation away from this model is penalized.
Equation (8) may be expressed as

$$\Psi(\mathbf{m}^*) = \left\| \mathbf{W}_{\mathrm{d}}^* \left[\mathbf{d}^* - \mathbf{f}^*(\mathbf{m}^*) \right] \right\|^2 + \alpha \left\| \mathbf{W}_{\mathrm{m}} (\mathbf{m}^* - \mathbf{m}_0^*) \right\|^2, \tag{9}$$

where α is a regularization parameter, $\mathbf{W}_\mathrm{m}$ is a weight (or roughness) matrix that defines the spatial extent and nature of smoothing between each parameter and its neighbors, and $\mathbf{m}_0^*$ is a reference parameter vector, not necessarily uniform. Penalizing relative to a reference vector can be removed by assigning $\mathbf{m}_0^*$ to the null vector. Similarly, smoothing between adjacent parameter blocks can be avoided by making $\mathbf{W}_\mathrm{m}$ a unit diagonal matrix.

The weight matrix $\mathbf{W}_\mathrm{m}$ may be constructed to permit anisotropic smoothing, for example, forcing greater horizontal smoothing than that in the vertical. The vector $\mathbf{m}_0^*$ may be expected values of log conductivity within the region or may be the result of a previous inverse model—the latter is useful for study of temporal changes with time-lapse data. The second penalty term in equation (8) may then be viewed as a means to incorporate a priori information into the inversion. The principle role, however, is to stabilize the inversion. Care must be taken when applying these terms, in some cases, for example, a smooth model, although stable, may be inappropriate (e.g., layered media where adjacent layers have vastly different resistivity).

Regularization of this type has been well established in the literature (Tikhonov and Arsinen, 1977); however, the work of deGroot-Hedlin and Constable (1990) brought wider appreciation through their applications to magnetotelluric data and coined the term *Occam's inversion*. Numerous variants on this approach have been used since.

Minimization of equation (9) may be achieved through application of gradient search methods. Using the Gauss Newton approach, minimization of equation (9) results in the iterative equations (Kemna and Binley, 1996; Kemna, 2000):

$$\begin{aligned}&\left(\mathbf{J}_k^{*\mathrm{H}}\mathbf{W}_\mathrm{d}^{*\mathrm{H}}\mathbf{W}_\mathrm{d}^*\mathbf{J}_k^* + \alpha\,\mathbf{W}_\mathrm{m}{}^\mathrm{T}\mathbf{W}_\mathrm{m}\right)\Delta\mathbf{m}_k^*\\ &\quad= \mathbf{J}_k^{*\mathrm{H}}\mathbf{W}_\mathrm{d}^{*\mathrm{H}}\mathbf{W}_\mathrm{d}^*\left[\mathbf{d}^* - \mathbf{f}^*(\mathbf{m}_k^*)\right]\\ &\qquad- \alpha\,\mathbf{W}_\mathrm{m}{}^\mathrm{T}\,\mathbf{W}_\mathrm{m}\left(\mathbf{m}_k^* - \mathbf{m}_0^*\right)\\ &\mathbf{m}_{k+1}^* = \mathbf{m}_k^* + \Delta\mathbf{m}_k^* \qquad k = 1,2,3,\ldots.\end{aligned} \tag{10}$$

In equation (10), $\mathbf{J}_k^*$ is the complex Jacobian (or sensitivity) matrix evaluated for the current model $\mathbf{m}_k^*$. This matrix may be computed using the principle of reciprocity (Geselowitz, 1971) as described in detail by Kemna (2000). The solution of equation (10) may be obtained by direct or iterative methods, the latter being preferred for large problems. Zhang et al. (1995) show, for DC resistivity inversion, that it is not necessary to form the entire Jacobian matrix for conjugate-gradient type solutions, and thus, significant storage restrictions are avoided. Similar algorithms can be applied to the general complex resistivity problem.

Satisfactory solution of equation (10) is dependant on appropriate assignment of regularization parameter α and data errors in $\mathbf{W}_\mathrm{m}^*$. The two terms are implicitly linked (see LaBrecque et al., 1996). Whereas a number of studies have adopted fixed values of the regularization parameter, in the approach of deGroot-Hedlin and Constable (1990), a search is made at each iteration k of the solution of equation (10) to find the optimum value. As the iterative procedure progresses, the value of α decreases as data misfit becomes more dominant towards the end of the iterative search.

Underestimation of data noise will result in poor convergence or significantly rough images. Overestimation of data noise will result in overly smooth images with degraded sensitivity and resolution. LaBrecque and Ward (1990) proposed a scheme that allows reweighting of data during the iterative process in equation (10). Morelli and LaBrecque (1996) have shown how this scheme may be used for 3D DC resistivity ERT. Kemna (2000) utilized this scheme for 2D complex resistivity inversion and further incorporated a means of accounting for phase angle errors in the complex inversion.

Alternative inversion approaches

The literature contains a number of apparently different schemes to invert ERT data; however, most follow essentially the same components as above. Examples of 3D resistivity inversion can be found in Park and Van (1991), Ellis and Oldenburg (1994), Sasaki (1994) and Lesur et al. (1999). A number of more significant modifications to the general procedure are worth noting, however.

Quasi-Newton approximation

One modification to the general approach, which still utilizes a regularized gradient search solution but incorporates an approximated Jacobian matrix, has been widely used for surface imaging. Since the formation of the Jacobian matrix in equation (10) accounts for much of the computational effort in any Gauss-Newton type inverse procedure, attempts have been made to minimize computational costs by using approximations to the sensitivity coefficients in quasi-Newton schemes. Loke and Barker (1995) describe such a scheme that has proved useful for imaging using only surface deployed electrode arrays. Although no attempts to follow such procedures for the general ERT case are apparent in the literature, it is likely that these approximations would be unsatisfactory due to the high contrasts in resistivity encountered using borehole electrode arrays.

Stochastic inversion

Another variant of the Occam's type approach has been devised which replaces the regularization matrix with a data covariance matrix. The stochastic inversion method, often called the maximum-likelihood method (Zhang et al., 1995), seeks to maximize the a posteriori probability density function of model parameters. Although the method itself is very general, all of the implementations of this method for ERT rely on several rather restrictive assumptions:

- The data errors and the parameters themselves are stationary, random variables
- Both the data errors and the parameters have normal (Gaussian) distributions
- The data errors are uncorrelated with known variances
- The parameters have known covariance, which depend only on the distance between the physical locations of the parameters; in other words adjacent cells are strongly correlated, distant cells poorly correlated

With these assumptions, maximizing the a posteriori probability density function is equivalent to minimizing the objective function given by

$$\begin{aligned}\Psi(\mathbf{m}^*) = {} & (\mathbf{d}^* - \mathbf{f}^*(\mathbf{m}^*))^H \mathbf{C}_D^{-1}(\mathbf{d}^* - \mathbf{f}^*(\mathbf{m}^*)) \\ & + (\mathbf{m}^* - \mathbf{m}_0^*)^H \mathbf{C}_M^{-1}(\mathbf{m}^* - \mathbf{m}_0^*)\,, \qquad (11)\end{aligned}$$

where $\mathbf{C}_D$ is the data noise covariance matrix and $\mathbf{C}_M$ is the model parameter covariance matrix (Tarantola, 1987; Yang and LaBrecque, 1999). This is very similar to equation (9) with $\mathbf{C}_D$ being equal to the inverse of the matrix $\mathbf{W}_\mathrm{d}^{*\mathrm{H}}\mathbf{W}_\mathrm{d}^*$. In much of the work on stochastic inversion, the parameters are assumed to be uncorrelated. In this case, equation (11) can be reduced to the same form as equation (9) and solved using the system given in equation (10). Although this is not a particularly reasonable assumption, it greatly simplifies the computation of the equation. In fact, the framework of stochastic inversion would provide little more than a formal method of choosing the values of the terms of $\mathbf{W}_\mathrm{m}^\mathrm{T}\mathbf{W}_\mathrm{m}$.

A more reasonable estimate of parameter covariance yields a large (often over 10^9 elements for large 3D problems), full matrix for $\mathbf{C_M}$. Yang and LaBrecque (1999) give an alternate solution method that avoids the direct inversion of this large matrix:

$$\begin{aligned}&\left(\mathbf{C}_M \mathbf{J}_k^{*\mathrm{H}} \mathbf{C}_D^{-1} \mathbf{J}_k^* + \mathbf{I}\right) \Delta \mathbf{m}_k^* \\ &= \mathbf{C}_M \mathbf{J}_k^{*\mathrm{H}} \mathbf{C}_D^{-1} \left(\mathbf{d}^* - \mathbf{f}^*(\mathbf{m}_k^*)\right) + \left(\mathbf{m}_0^* - \mathbf{m}_k^*\right). \qquad (12)\end{aligned}$$

The result, is a nonsymmetric system which, though less efficient than the symmetric system of equation (10), can still be solved fairly efficiently using iterative methods such as the quasi-minimum-residual-biconjugate-stable algorithm (QMRCGSTAB). Yang and LaBrecque (1999) found that the stochastic inversion routine required about twice the computation time of an Occam's inversion routine that used the same forward algorithm and the same algorithms to create the sensitivity matrix.

Regardless of the inversion method, ERT tends to show poor sensitivity in the center of 3D volume away from the electrodes. However, Yang and LaBrecque (1999) found that this problem appeared to be much more severe for the unmodified stochastic inversion algorithm than for the comparable Occam's inversion algorithm. In both analysis of field data and synthetic model studies, the stochastic algorithm was unable to reconstruct 3D features located in the center of the volume between wells. It is important to note that the models used in the study contained layered sequences and strongly contrasting 3D anomalies that clearly violated the underlying assumption of stationary, Gaussian-distributed parameters. To overcome this problem and provide more uniform image quality, Yang and LaBrecque (1999) used an empirical scheme from Morelli and LaBrecque (1996) to alter the parameter standard deviations:

$$\sigma'_{ik} = \alpha\, \sigma_{ik} \left\{ \mathrm{diag}\left(\mathbf{J}_k^{*\mathrm{H}} \mathbf{J}_k^* \right)_i \right\}^{-n}, \qquad (13)$$

where σ_{ik} is the a priori standard deviation of ith model parameter, σ'_{ik} is the model standard deviation after applying the empirical correction, α is an empirical factor defined as in equations (9) and (10), and n is an empirical weighting factor which ranges from 0.10 to 0.30.

The method removes one disadvantage of the stochastic method in dispensing with the formal framework for picking the weights within the parameter covariance matrix. Overall, the method of Yang and LaBrecque produces images comparable to those of Occam's methods though requiring considerably more computational effort.

Decoupled DC resistivity—Induced polarization inversion

The complex resistivity inverse model in equation (10) requires data in the form of complex impedances, normally measured as magnitude and phase angle (frequency domain). There is an alternative approach that is acceptable as long as the IP effects (imaginary part of the impedance for frequency domain, or off-time voltages for time-domain chargeability) are very small compared to the normal (real or on-time) voltages. In this approach, the induced polarization can be estimated as a linear perturbation of the normal, real resistivity forward model, and the induced-polarization effect can be estimated using the Jacobian given in equation (10) (LaBrecque, 1991; Li and Oldenburg, 2000).

In this approach the DC resistivity problem is first solved, and then, using the image of resistivity, a linearized gradient search is made to determine an image of chargeability that is consistent with the observed IP response. Oldenburg and Li (1994) propose a more general nonlinear approximation to the problem and show the effectiveness for 2D surface arrays. This uncoupled solution is more comparable to the general complex resistivity problem defined earlier.

Inverting time-dependent data

One of the main strengths of ERT is that resistivity (and induced polarization, to a degree) is dependent on hydraulic, chemical, and thermal changes in the subsurface. Thus, monitoring natural or artificially induced changes in resistivity can often provide valuable information about flow and transport processes, including the effectiveness of remediation strategies for clean up of contaminated sites (as shown later).

To assess changes in ERT images with time, it is clearly possible to simply carry out independent data inversions, each representing a snapshot by the "impedance camera" at different times during the processes. By subtraction of pixel values from some reference, or background, image changes are easily computed. However, in many cases changes may be very small in comparison with the natural spatial variability within the region of interest. A cross-borehole survey in near-surface sediments may reveal contrasts over several orders of magnitude, for example, whereas an increase or decrease in saturation in the vadose zone, say, due to some process may change the resistivity by only a few percent. Since the inversion process is strongly influenced by data errors, the subtraction of independent images may then reveal little about the process of interest.

To image small changes in a background of large contrasts, attempts have been made to invert for changes in resistivity using coupled data sets. Clearly, from examination of the objective function in equation (9) or equation (11) a reference parameter set $\mathbf{m}_0^*$ may be used to constrain the inversion against some reference state. LaBrecque and Yang (2000) developed a modification of this approach using what they call *difference inversion,* which also incorporates a modified data vector formed from differences in measurements at two time levels. Their approach not only conditions parameter estimates on some background state but also significantly reduces computational effort in the inversion—an aspect that is essential for real-time process control, as shown later in the steam flood case study .

A more common approach utilizes a ratio of two impedance data sets in the inversion. In this method, a new data vector $\mathbf{d}_r^*$ is formed from

$$\mathbf{d}_r^* = \frac{\mathbf{d}_t^*}{\mathbf{d}_0^*}\mathbf{f}^*(\sigma_{\mathrm{hom}}^*), \tag{14}$$

where $\mathbf{d}_0^*$ is the data vector at some reference state, $\mathbf{d}_t^*$ is the data vector at some time t and σ_{hom}^* is an arbitrarily chosen homogenous conductivity.

Inversion of the new data set $\mathbf{d}_r^*$ in the normal manner then results in an image that will reveal changes relative to the reference value σ_{hom}^*. Most applications of this approach have been in DC resistivity problems (see Daily et al., 1992; Ramirez and Daily, 2001); however, it may also be applied to the general complex resistivity problem. In fact, for polarization problems, frequency, rather than temporal, effects may be of wider interest.

This "ratio" approach has proven to be invaluable for many ERT applications, in particular when 2D inversions are applied to 3D problems. Borehole effects due to overly conductive or resistive backfill, commonly observed in images of cross-borehole data are often removed by such a transformation. More importantly, however, changes in the data (and their errors) are easily transformed into the input of the inversion process.

Image resolution

ERT image resolution is a complicated function of many factors including the regularization scheme used, the parameter block size, data signal-to-noise ratio, electrode array geometry, measurement scheme, and the resistivity distribution. The resolution matrix **R**, formally defined as

$$\mathbf{R} = \left(\mathbf{J}_k^{*\mathrm{H}}\mathbf{W}_{\mathrm{d}}^{*\mathrm{H}}\mathbf{W}_{\mathrm{d}}^{*}\mathbf{J}_k^{*} + \alpha\,\mathbf{W}_{\mathrm{m}}^{\mathrm{T}}\mathbf{W}_{\mathrm{m}}\right)^{-1} \mathbf{J}_k^{*\mathrm{H}}\mathbf{W}_{\mathrm{d}}^{*\mathrm{H}}\mathbf{W}_{\mathrm{d}}^{*}\mathbf{J}_k^{*}\,, \tag{15}$$

may be computed to assess the extent of smoothing caused by the regularization and how each pixel parameter value is constrained by the data. In an ideal case, **R** will be the identity matrix—indicating perfect resolution of the entire model—in practice, it will differ significantly from this. The deviation of a diagonal term in **R** from unity indicates an increasing volume averaging effect on the determination of the corresponding parameter. Off diagonal terms in **R** may be used to display the effect of smoothing on each parameter (see for example, Alumbaugh and Newman, 2000), but normally only the diagonal of **R** is used, as in Ramirez et al. (1993, 1995), in this case using a scaled function of the diagonal of **R**.

Unfortunately, the computation of **R** is numerically intensive. Furthermore, iterative solvers used for large 3D inverse solutions are inefficient for such multiple right-hand-side matrix vector solutions. Consequently, many large-scale applications of ERT often fail to report on the characteristics of the resolution matrix. Because of the computational burden in forming **R**, Park and Van (1991), for the DC resistivity problem, used the matrix product ($\mathbf{J}^T\mathbf{J}$), which is easily computed, to assess spatial sensitivity in the inversion. The use of such a quantity was also recognized by Kemna (2000) in his development of 2D complex resistivity inversion procedures. Kemna computed the vector,

$$\mathbf{r} = \left(\mathbf{J}_k^{*\mathrm{H}} \mathbf{W}_\mathrm{d}^{*\mathrm{H}} \mathbf{W}_\mathrm{d}^{*} \mathbf{J}_k^{*} \right), \tag{16}$$

as a surrogate for the diagonal of **R**, where k is the final iteration of the inversion. The vector **r** will show high values where sensitivity of the measurements is greatest and low values where smoothing terms in the inversion will be more influential. Figure 3 shows a comparison of the two approaches for a 2D DC resistivity inversion carried out at as part of a characterization program in the vadose zone of a sandstone aquifer (Binley et al., 2001b). In Figure 3a the inverted resistivity structure is shown, from which a distinctly layered environment is apparent (in this case caused by contrasting fine and medium grained sediments). In Figure 3b the diagonal of the resolution matrix **R** is displayed indicating high image resolution close to electrode sites, which for this example are located in boreholes and on the surface. Figure 3c shows how the vector **r** in equation (16) shows similar characteristics. In this case the effect of conductive layers (including a relatively conductive near surface) on measurement sensitivity can be seen clearly.

An alternative procedure for characterizing image resolution is the depth of investigation (DOI) index proposed by Oldenburg and Li (1999). In this approach the objective function in equation (9) is minimized for two different reference parameter sets, $\mathbf{m}_{0a}$ and $\mathbf{m}_{0b}$; the difference between the final model from these two inversions ($\mathbf{m}_a$ and $\mathbf{m}_b$, respectively) is then used to determine the index for each parameter block i using

$$\mathrm{DOI}_i = \frac{\left| m_{a,i} - m_{b,i} \right|}{\left| m_{0a,i} - m_{0b,i} \right|}. \tag{17}$$

In areas of the image where sensitivity is low, the index DOI will be close to unity, revealing regions where the final model is weakly constrained by the measurements. Similarly, low DOI values will indicate high sensitivity and consequently allow greater faith in modeled values. Although this approach has only been applied to surface imaging problems, the generalized nature of the concept permits utilization to any electrode geometry. For more discussion on image resolution see Jackson (1972), Aki and Richards (1980), and Vasco et al. (1997).

Case Histories

We now present some case histories to illustrate the potential value of ERT for subsurface imaging. Our objective is to show the flexible nature, and identify potential areas of weakness in the technique. This collection represents a small fraction of many investigations where the method has been used successfully. The examples have been selected in order to cover a wide variability of imaging capabilities, illustrating both temporal and spatial resolution and showing the range of scales, environments, and processes (natural and artificial) to which ERT has been applied successfully.

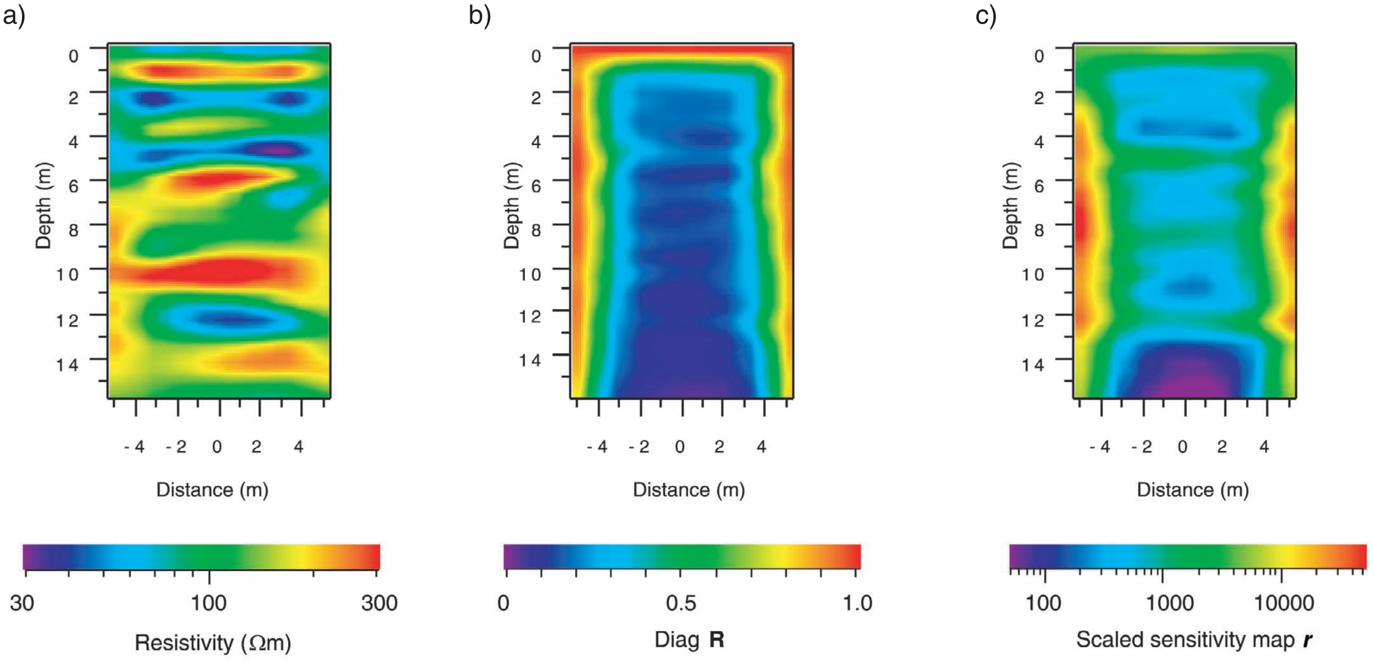

Figure 3. Illustration of ERT resolution estimation for a 2D DC case. (a) Final resistivity model, (b) diagonal of resolution matrix **R** in equation (14), and (c) sensitivity map **r** in equation (16).

Unexploded ordnance (UXO) detection

Locating unexploded ordnance has become a serious problem, especially on military bases that are being closed so that the lands can be returned to public use. UXO targets can range from small arms ammunition to large bombs, and may be neatly staked before burial, or may be scattered over a large area. Often the goal is a rapid reconnaissance of large areas, and for this use, ERT is not particularly useful because of the need for electrical contact with the ground. For reconnaissance applications, magnetometry or electromagnetic induction methods have proven useful. However, these traditional methods fail when investigating the subsurface beneath buildings or other structures that have structural metal close to the ground.

The U. S. Navy, at the former Mare Island Base near Vallejo, California, must search for UXO that may have been buried under ordnance assembly buildings before the buildings were constructed. ERT was tested as a possible method to accomplish this. Of course, most ordnance is metal cased and will be more electrically conducting than soils. However, relatively high conductivity was not the diagnostic thought most likely to identify the UXO, because this effect would be difficult to separate from natural heterogeneity in the soil conductivity (Daily et al., 2000). Instead, the signal of interest was the polarization induced at the metal-soil boundary, known in geophysics as *electrode polarization* (Van Voorhis et al., 1973).

The phase difference between the applied current and measured voltage provides information about the electrical polarizability of the soil and is sensitive to soil type (Marshall and Madden, 1959), but also the presence of metal (Van Voorhis et al., 1973). It is the latter that is of interest for UXO detection. The strategy, therefore, is to reconstruct phase tomographs and identify large negative phases that may be associated with the presence of buried metal. To be useful, however, the phase anomalies due to buried metal must be discriminated from the phase anomalies due to other polarization sources from certain soil types such as clay.

To test the utility of ERT to locate UXO and discriminate its IP signal from that produced by soil, a test site was chosen with representative soil types. At this site an assortment of UXO, taken from other locations at Mare Island, were buried at 1–2 m depth. About 10 kg of assorted material (from metal fuses about 1 cm diameter and 10 cm long to shell casings about 20 cm diameter and over 30 cm long) were buried in the same condition as originally exhumed, except for being rendered inert. After the soil in the hole was compacted, the site was left undisturbed for about 3 weeks before the ERT measurements began.

A 2D array of 30 copper-copper sulfate electrodes [which have a low intrinsic polarization (see Keller and Frischknecht, 1966)] was placed on the ground surface over the buried target as might be used if electrodes could be placed underneath a building (most buildings of interest at Mare Island stand on pillars about 1 meter above the ground surface). The results of 3D inversion of a volume beneath the array are shown in Figure 4.

The impedance magnitude, or resistivity, reconstruction shows natural variations over the image block that are probably due to variations in soil type, compaction, moisture content, pore water salinity, etc. There is no evidence of a conductive anomaly associated with the UXO that is distinguishable from this natural variation. The phase reconstruction, on the other hand, shows an anomaly of –15 mrad close to the buried mass in an otherwise relatively uniform background of –3 to –5 mrad. The depth of the reconstructed anomaly is very close to what we expect although the lateral position is displaced 0.3 to 0.6 m. This error could be from smoothing done by the inverse algorithm, or from data errors, or simply from inaccuracies in the positioning of the UXO mass boundaries.

This controlled test was encouraging and Daily et al. (2000) report another successful controlled test similar to the one reported here. Unfortunately, these tests were not fully conclusive because a blind test, conducted under a building without prior knowledge of what was buried, produced large phase anomalies that did not correlate with UXO locations. Clearly, this work is encouraging but more development is needed to discriminate between IP anomalies caused by UXO and those caused by other conditions. Perhaps, for example, the spectral IP generated by the metal in UXO is unique from that produced by natural geologic sources of IP.

Characterization of municipal landfills

A significant amount of data has now been acquired over a variety of buried landfills, confirming a correlation between buried waste and IP effects. In delineating landfills, ERT often has significant advantages over several other geophysical methods, including greater flexibility in depth of investigation than ground penetrating radar and better vertical resolution than most existing conductivity systems. In addition, IP measurements have also been successful at delineating buried waste that is nonmetallic and could not be detected with a magnetometer.

A comparison of ERT data, collected using surface electrodes only, over a typical background area without waste and an area subsequently proven to contain buried waste is shown in Figure 5 (taken from Carlson et al., 1999). Both lines of data are from the Rio Nuevo North Landfill in Tucson, Arizona. Lines are approximately 425 m apart. Figure 5a shows the IP and resistivity inversions for the background area (called line 180). Notice that all IP chargeability values are less than 2 ms, and resistivity data are relatively layered. In Figure 5b, however, an IP anomaly is clearly evident in the central portion of line 450, and this area has since been confirmed as containing

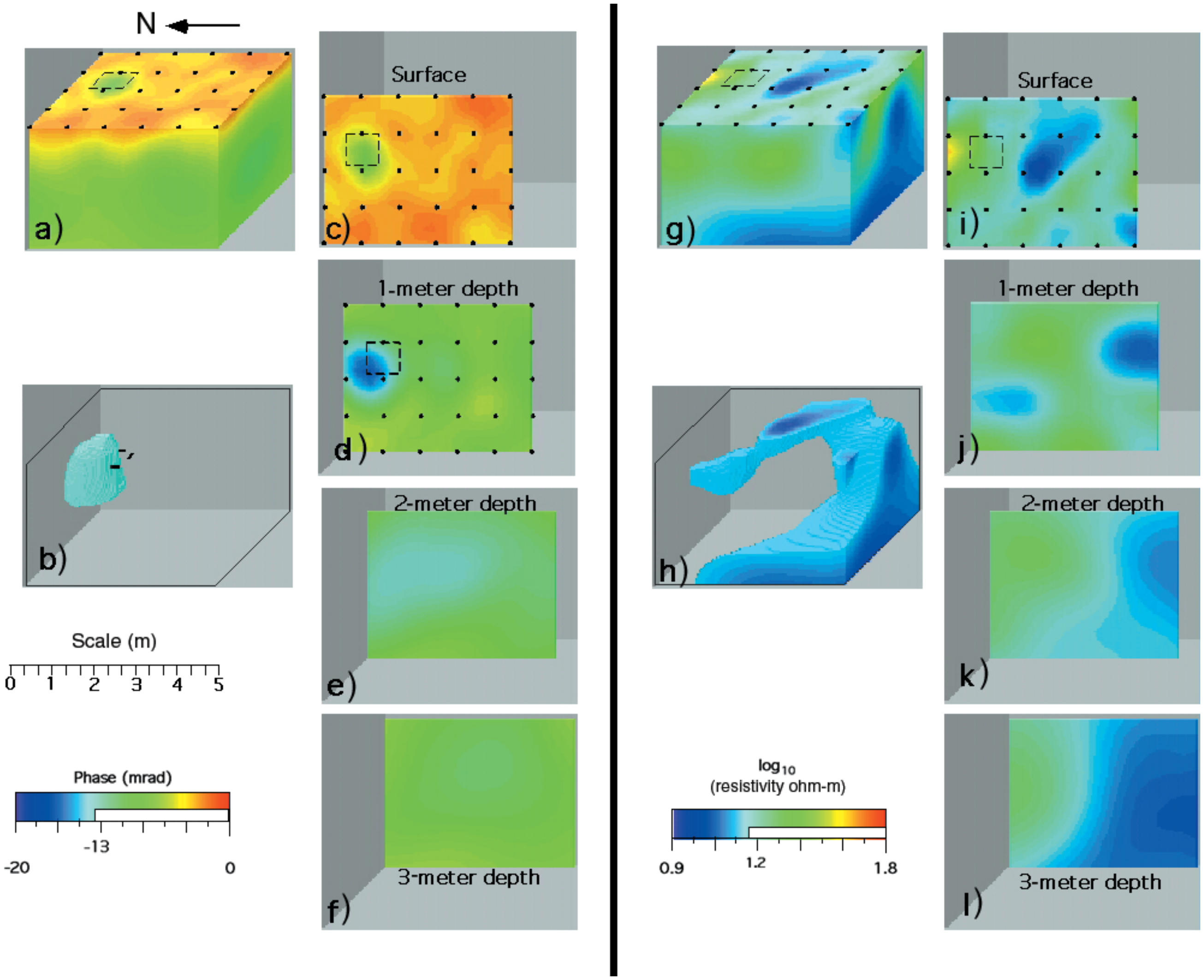

Figure 4. Three-dimensional impedance tomograph for a controlled test at Mare Island. Impedance phase [parts (a) through (f)] and impedance magnitude [parts (g) through (l)]. The UXO is buried under the dashed square. There are two voxels between adjacent electrodes and the measurement frequency is 0.25 Hz. (a) Phase in milliradians (mrad) in the reconstruction block. (b) Reconstruction volume in part (a) is rendered transparent between 0 and –13 mrad, and the buried mass of UXO is imaged as a phase anomaly between –13 and –20 mrad. (c)-(f) Plan view sections of the reconstruction block. (g) Impedance magnitude in ohm-m in the reconstruction block. (h) Reconstruction volume is rendered transparent between 16 and 63 ohm-m. (i)-(l) Plan views of depth sections in the reconstruction block.

buried waste with approximately 3 m of soil cover. Note also that the DC resistivity data are very irregular and are not layered similar to line 180. Historical photographs from the 1950s and 1960s of the line 450 area indicate numerous pits and excavations from gravel operations.

A more extensive example can be seen in a compilation of all the Rio Nuevo North Landfill ERT data. Figure 6 (taken from Carlson et al., 1999) shows the grid of data in more detail on lots 17 and 18, with the interpreted waste outlined with a red dashed line. (Note that the interpreted outline of the waste is from the IP data at all depths.) Borings confirmed the outline of the waste based on the IP data, as well as the thickness of soil cover (> 4.5 m for most the anomalous area). Some borings were positioned very close to the edge of the anomaly to verify the resolution of the IP data, and in all cases, the IP data were confirmed.

Outside of the anomaly attributed to waste, several other anomalous areas were identified. In some cases, these anomalies could be attributed to other cultural features; the linear anomaly in the southeastern part of the grid on Figure 6 is an old utility line, for example. A weak, shallow anomaly near the northwestern edge of the grid was drilled, but no waste was found. This anomaly, and a small number of other small features, are attributed to possible clays or unknown cultural features.

This relationship between buried municipal waste and IP/resistivity has been relatively consistent on work at six different buried landfills, and is supported by 145 boreholes and trenches. At some sites, trenching had been done prior to the surveys, while numerous borings were performed after the surveys to confirm the geophysical work. Undisturbed background areas tend to show very small or no IP effects (< 1 or 2 ms) with layered or homogeneous resistivity. Disturbed areas with no subsurface waste tend to show very small or no IP effect also, but irregular resistivity (laterally and vertically). Areas of subsurface waste show well-defined IP anomalies (> 3 ms) and irregular resistivity. Both resistivity and induced polarization imaging have been shown to be important in locating the subsurface waste and reconciling the geophysical data with historical records.

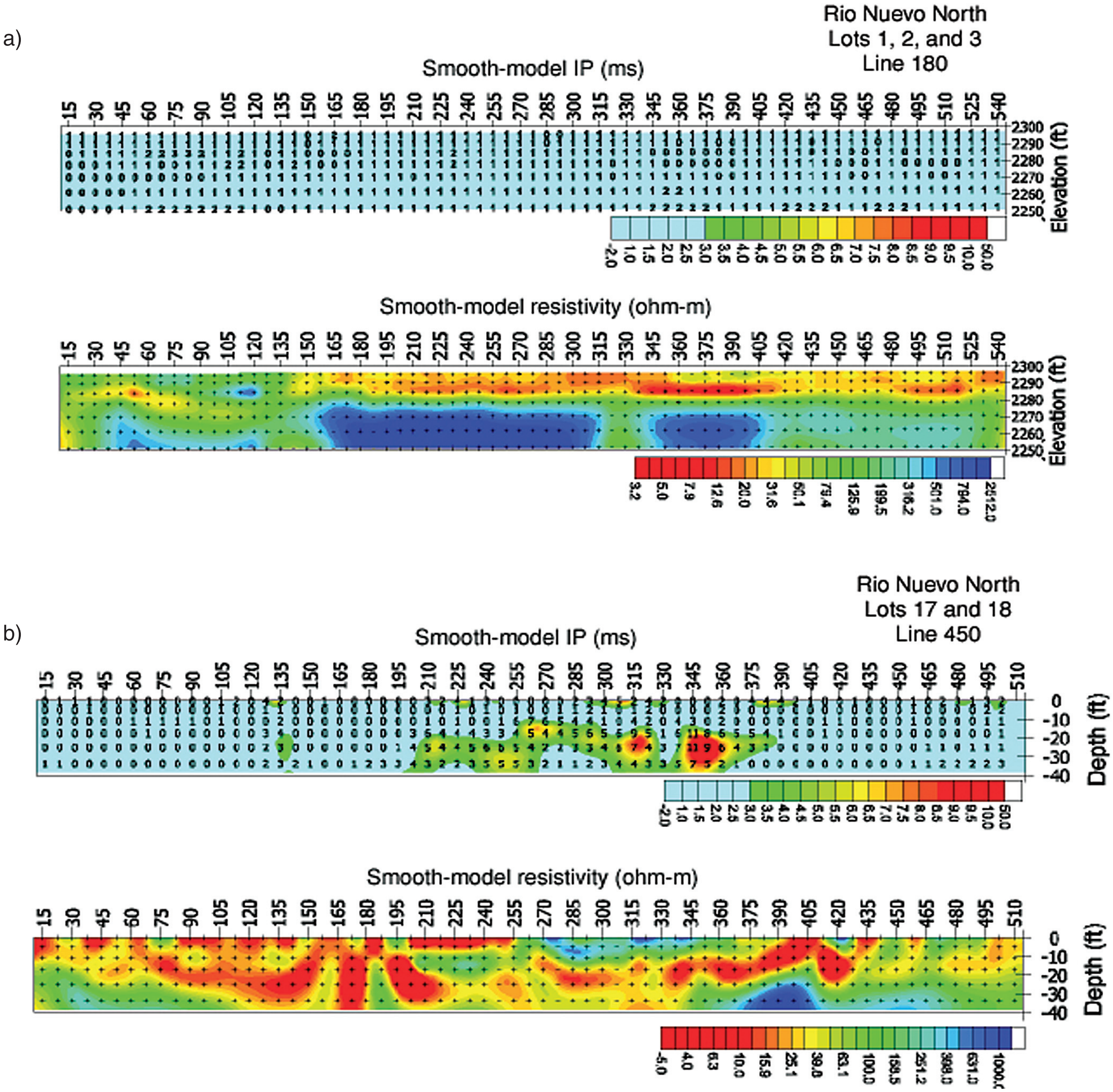

Figure 5. Resistivity and IP inversion (2D) for two surveys at the Rio Nuevo landfill site in Tucson, Arizona. (a) Inversion for the background area (lots 1, 2, and 3, line 180) where no waste is buried. (b) Inversion for a survey over the landfill (lots 17 and 18, line 450) where waste was confirmed buried (the central portion of the image) with approximately 3 m of soil cover. (taken from Carlson et al., 1999)

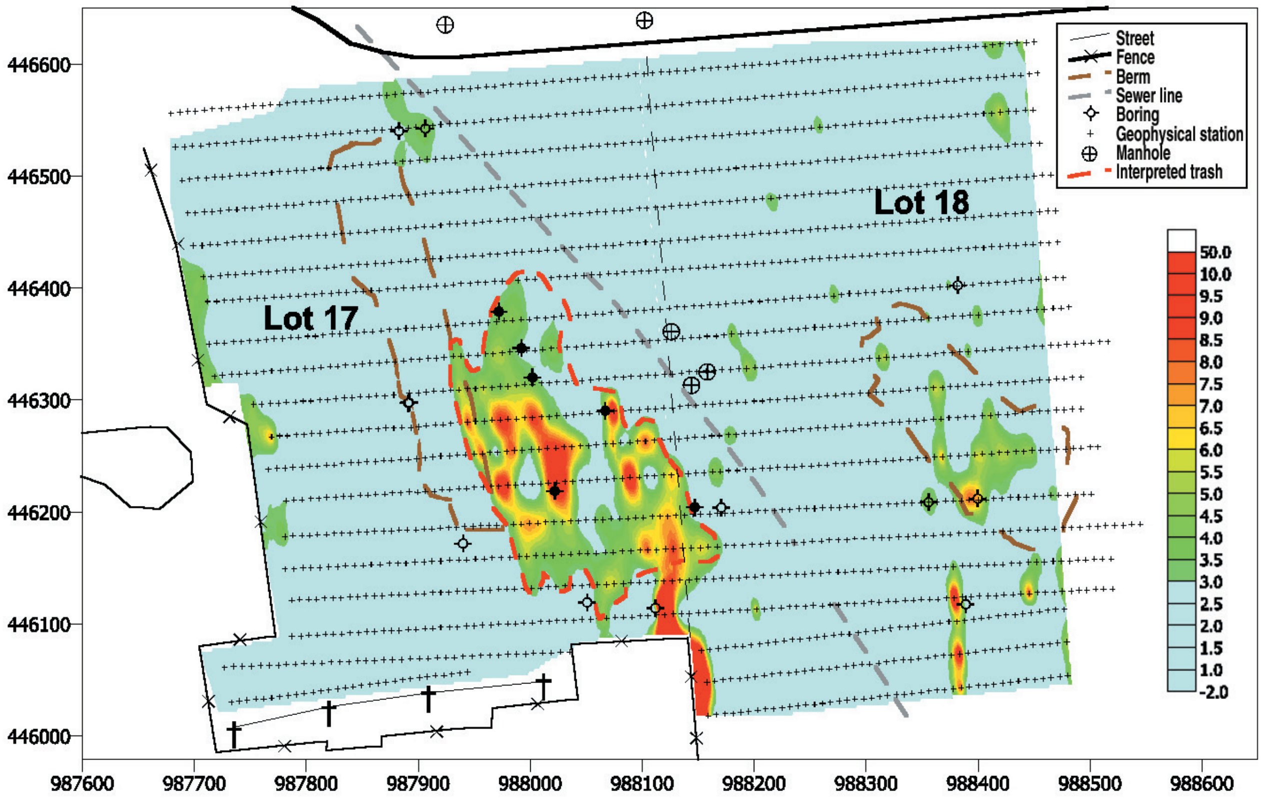

Figure 6. Plan view of the 2D IP inversion for the entire Rio Nuevo site at a depth of 6.1 m. These results required more than 14 000 measurements at 3767 locations along lines spaced 9.1 m apart (black dots). The dashed orange line outlines the interpreted waste location. (taken from Carlson et al., 1999).

Monitoring dynamic processes: Visalia Pole Yard steam injection

The Visalia Pole Yard is about 4 acres in size and was the site of a wood treatment plant from the 1920s through the 1970s. Operations resulted in both soil and groundwater contamination with creosote, pentachlorophenol, and diesel fuel to depths of 30 m. Through a collaboration between Lawrence Livermore National Laboratory (LLNL) and the California Edison Company, the site was used for a full-scale demonstration of one of the latest technologies for in-situ remediation, dynamic underground stripping (DUS).

With DUS, the temperatures of contaminated soils were raised to (or above) the boiling point of water throughout most of the site by injection of steam. At times, as much as 22 000 kg per hour of steam were injected. Air was co-injected with the steam and both vapor and liquids were aggressively extracted. During the 25 months of operation, a total of 512 000 kg of creosote were removed or destroyed in-situ (4700 kg/wk).

ERT was used at the site along with strings of thermocouples to monitor the movement of steam and overall temperature of the site. Previous work by Ramirez et al. (1993) showed that tomographs of resistivity could be used to monitor steam progress. The goal at the Visalia site was to provide this information both faster and at higher resolution than traditional hydrological monitoring. This meant that a great deal of data had to be collected, processed, and interpreted very quickly. In addition, the data had to be of good quality; there was no time to polish or reprocess data. This was complicated by the fact the site was often extremely noisy, containing numerous power systems, pipes, boilers, and metal wells.

Although there were significant challenges, there were also some significant advantages in this environment. First, much of the emphasis here was on monitoring changes over time. It is easier to monitor changes than to measure absolute quantities. Second, the entire site was wired so that all data were collected from a single location.

Due to limitations in both the collection and interpretation capabilities at the time, data were collected and interpreted in 2D "planes," where a plane is the data collected between two wells. In a typical field day, 60 to 70 planes of data were collected. For a typical plane, there were 13 electrodes per well (26 electrodes total) and the system collected 598 data points. Hardware available at the time could collect four to five such data sets per hour.

Collecting a full set of data for the site took roughly 16 hours.

The site design required that all materials in the subsurface be able to withstand temperatures of at least 150°C. The electrodes consisted of short pieces of stainless-steel tubing fixed to temperature-resistant fiberglass rods, each electrode connected to the surface using a Teflon-coated cable. To place electrodes, a small-diameter steel tube with the electrode string placed in the center was pushed to depth with a cone-penetrometer (LaBrecque et al., 1995). The steel tubing was then removed leaving the electrode string and a disposable tip in the hole.

At Visalia, the goal was to provide interpreted ERT images within 24 hours of data collection. To achieve this, automated data processing was nearly as important as automated data collection. Figure 7 shows a graphical overview of the data processing system used at the site. As soon as a complete plane of data was collected, the ERT operator transferred the data file into the output folder and processing would begin while the next plane of data was collected.

Processing began by comparing reciprocal DC-resistance data values to provide a point-by-point check on system operation. The next step (Figure 7) was to add a unique header to the data file. This header controlled the inverse process, providing the finite-difference mesh, the locations and radii of nearby metal wells, and the locations of all of the electrodes. The file with the header appended was then placed in a process queue where it could be accessed by several processors. The first available processor then inverted the data contained in the file. When the inversion was completed, the processor placed the results back in the queue. In the final stage of processing, the inverse results were compared with the images for the background data set and several types of images were created. These included images of the absolute resistivity, the logarithm of the resistivity, the change in resistivity, and the percent change in resistivity from background. These images were sorted and stored separately for each image plane.

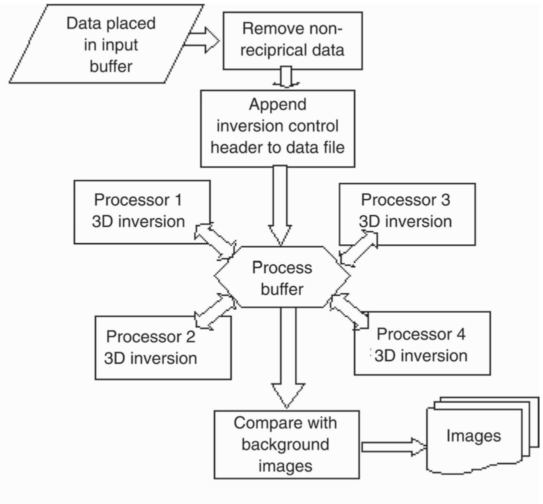

Figure 7. Chart showing flow of data during processing of the Visalia Pole Yard steam injection.

The 3D DC resistivity Occam's inversion routine of LaBrecque et al. (1995) was used to invert the data since the routine allows for incorporation of metal well-casings in the inversion routine. Figures 8 and 9 show examples of using ERT to monitor a rapidly changing steam front. In order to create steam within the subsurface, the formation must first be heated until the vapor pressure equals or exceeds the hydraulic head in the formation. For the injection depth at the site, this required heating the formation to about 110° C. Heating the fully saturated formation from ambient temperatures (about 20° C) to 110° C decreases the bulk resistivity by about a factor of three (see for example, Waxman and Thomas, 1974a). When the pore water is replaced by steam, the formation becomes desaturated and extremely resistive. By comparing images with background, it is then possible to track both the increase in temperature (decrease in resistivity) and the presence of a steam front (increase in resistivity).

Figure 8 shows the resistivity changes after steam injection had been stopped for approximately four weeks and then restarted. Data for this image were collected on the same day that steaming resumed. Due to the previous steam episode, the temperature of much of the site was still close to 100° C, but as yet, no distinct steam zone was present. Dark areas indicate areas where resistivity has more than doubled from that of the background images. The

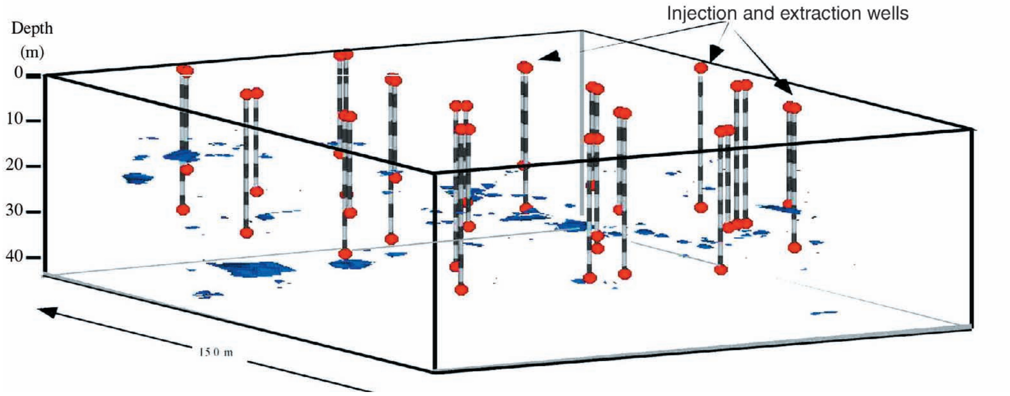

Figure 8. Visalia Pole Yard steam injection results. Three-dimensional composite of 60 planes of ERT data shown for the day when steam injection is resumed. Only those regions with increases of 90% or more of the background values are shown. Injection and extraction wells are also shown.

small, scattered anomalies do not represent steam but occur for several reasons. A number of them occur in close proximity to injection and extraction wells and may indicate changes in the formation or well grouting during the injection, or entrapped air that was injected with the steam. At least some of these anomalies occur due to noisy electrodes.

Images on the following day (Figure 9) show a relatively extensive steam zone that appeared literally overnight. The steam zone (shown as the dark zones in the figure) is relatively narrow and elongated indicating that it is following a preferential pathway. Over the next several days (not shown) the steam zone expanded somewhat but maintained essentially the same shape and orientation.

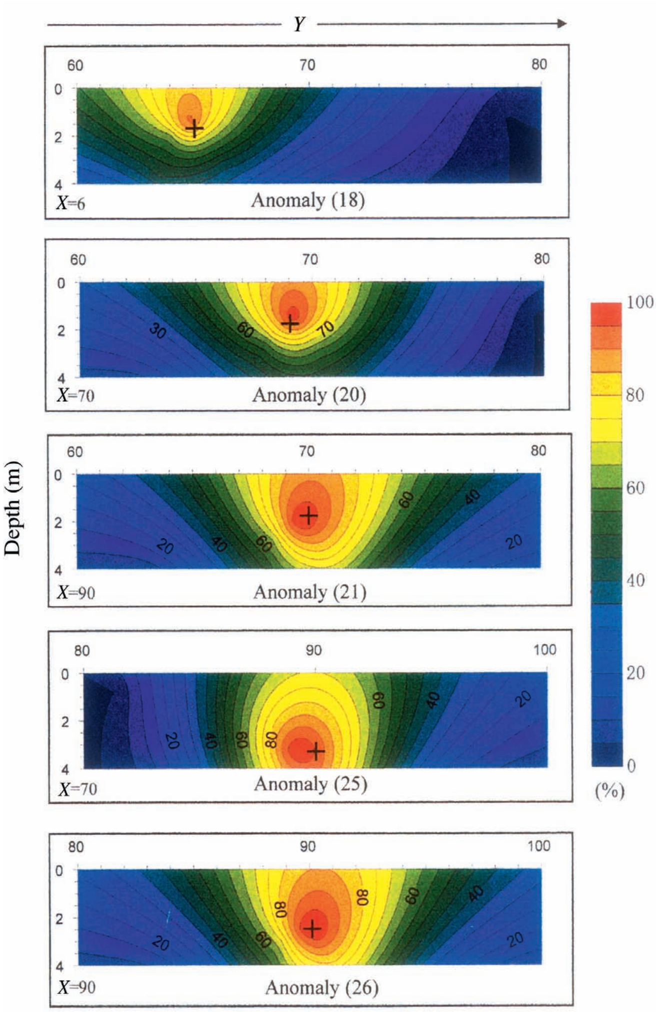

Figure 9. Visalia Pole Yard steam injection results. Three-dimensional composite of 60 planes of ERT data shown one day after Figure 8. Only those regions with increases of 90% or more of the background values are shown. Injection and extraction wells are also shown.

Monitoring leakage from underground storage tanks

In 1994 and 1995, field experiments were conducted under a 15 m diameter steel tank mockup located at the Hanford Reservation, Washington, to evaluate the capabilities of ERT to detect leaks from large metal storage tanks; the details of this work can be found in Ramirez et al. (1996). Both government and industrial activities require thousands of storage tanks for fuels, solvents, and other chemicals. The test reported here was designed specifically to address the issues of leaks from the single shell tanks built by the U.S. Department of Energy during the cold war for storage of highly radioactive mixed wastes. The contents of these tanks are typically highly saline liquids and therefore electrically conductive. The ERT method employed by Ramirez et al. (1996) was based on mapping the resistivity around and below a tank mockup. The hypothesis was that spilled liquids change the electrical resistivity of the soil in a measurable way, and that electrical resistivity tomographs can be used to map the resistivity changes. This strategy required that prespill measurements be available so that the prespill and postspill resistivities could be compared.

The presence of a metal tank with a resistivity of approximately 10^{-8} ohm-m embedded in soil with a resistivity of 10^2 to 10^3 ohm-m results in resistivity contrasts that are much larger than those found in most natural geologic settings. One consequence of this large contrast is that a large fraction of the electrical current transmitted during a survey is shunted through the metal tank. Furthermore, voltage gradients caused by the presence of conductive anomalies in the soil are flattened by the proximity of the tank. Both of these effects contribute to a significant reduction in the sensitivity of the measurements to the soil properties and in the ability to resolve the anomalies. Also, many of the assumptions made in formulating the forward and inverse problems are only valid for smaller electrical contrasts.

The field experiments were performed under a 15.2 m diameter steel tank mockup located at the Hanford Reservation (200 East Area) near Richland, Washington. Figure 10 shows that sixteen boreholes with eight electrodes in each surrounded the tank, the bottom of which was 1.5 m below grade. The electrodes were located in 10.7 m deep boreholes starting at the ground surface and spaced every 1.52 m. The diametrical distance between boreholes was 20.7m.

ERT data surveys were collected in each of eight horizontal planes beneath the tank, before and during a brine release. Plane 8 is a horizontal cross-section at the ground surface 1.5 m above the bottom of the tank (so it contained the tank itself). Plane 7 is 1.5 m lower, a cross-section level with the tank bottom. Plane 6 is 1.5 m below the tank bottom, and so on to plane 1 which is 10.7 m below the ground surface. This arrangement provided a series of 2D image planes at many levels which, when assembled together, gave an overall 3D view of the plume formed beneath the tank during the release and which could be used to determine the effects of imaging current shunted through the tank bottom. To calculate the changes in the soil's electrical resistivity, data from when the plume caused by a tank release is present were compared with a corresponding data set measured for the case when there is no plume [see equation (14)].

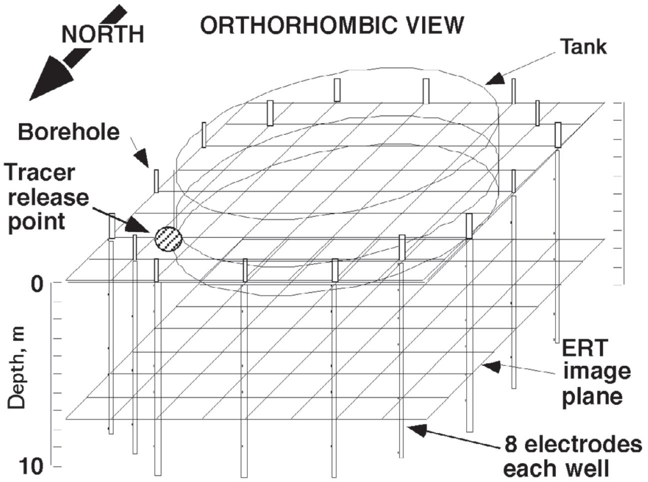

Figure 10. Schematic of experimental set up for leak detection. A 15-m diameter steel tank shell, the lower 1.5 m of which is buried, is surrounded by 16 boreholes with 8 electrodes in each. Eight electrodes at a common depth are used for each ERT image plane.

Figure 11 presents two-dimensional tomographs collected during the course of a salt water (conductivity 3 S/m) release of 3970 liters. The location of the release point is on the side of the tank as indicated on the figure. Each column of images shows the changes detected for a given time at various depths; the depth of images on each column increases from top (0 m depth) to bottom (10.7 m depth). The images for 27 July, after injecting 1200 l of brine, show clearly detectable electrical conductivity increases directly below the release point between 3.0 and 7.6 m depth. This suggests that the brine is moving almost straight down as may be expected in reasonably homogeneous sandy soil present at the site. Note that the changes observed increase in magnitude as time and released volume increase. Also, note that the bottom of the changing region deepens as time increases. The resistivity decreases become stronger over time implying that the flow paths are becoming more saturated with salt water. The position of the flow paths also appears to be stable over the period of the experiment.

This experiment used highly conducting salt water that provided a very good electrical tracer for ERT. Other fluids will provide different contrasts and therefore yield different sensitivities. However, the conditions for the work reported here (Ramirez et al., 1996) demonstrated that, despite the interference of the metal tank, ERT can be used to not only detect the presence of a leak, but also can be

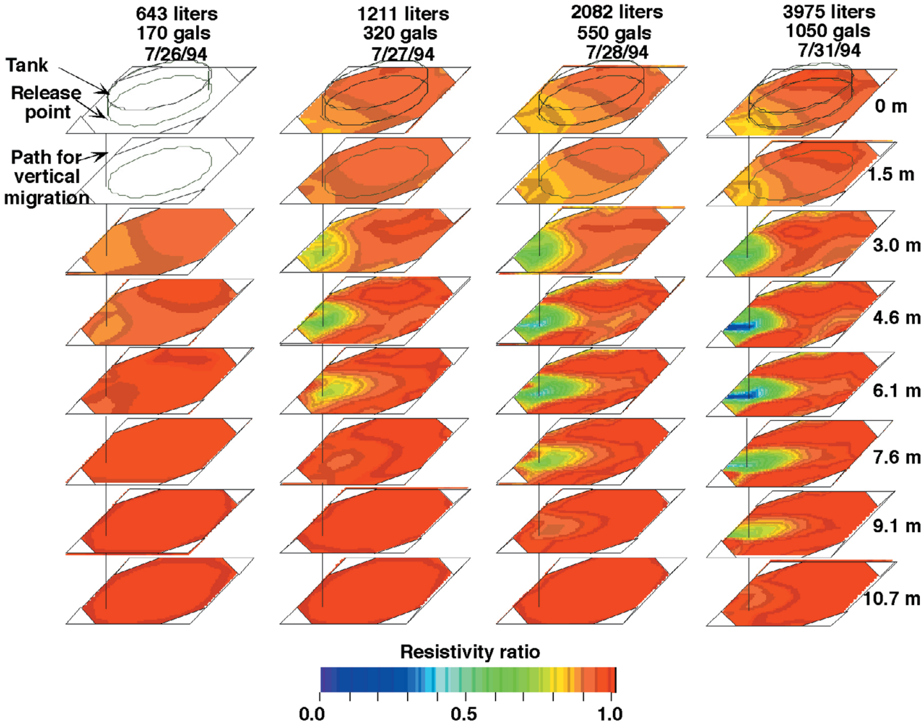

Figure 11. A series of 2D ERT tomographs which show how the electrical resistivity of the soil decreases during a side release of 3970 l of brine. When the resistivity ratio is 1.0 the resistivity is not changing—a ratio less than 1.0 indicates a resistivity decrease. The vertical lines show the trajectory the brine would follow if it moved straight down.

useful to locate its source and estimate the size and migration of the associated plume. Of course, in actual application, a tank may have a long history of leaking before this method is used to detect the leak. Rameriz et al. (1996) also show that very slight changes in an existing plume can also be detected and used to determine if a tank continues to leak.

Imaging preferential flow and transport of solutes in soil and rock cores

One of the earliest geophysical applications of ERT was that of Daily et al. (1987) in a study of flow processes in laboratory samples of fractured Topopah Spring Tuff from Yucca Mountain, Nevada (see also the following case study). In this lab scale study Daily and colleagues used relatively simple imaging tools based on backprojection techniques developed for biomedical applications. Nevertheless, this early work demonstrated the potential value of ERT to assist in the hydraulic characterization of flow and transport in laboratory scale samples and thus aid in improving conceptual and mathematical models of in-situ processes.

Binley et al. (1996) extended the work of Daily et al. (1987) in their study of solute transport in undisturbed soil cores, in order to assess preferential flow pathways in natural soil structures. For this study, soil cores approximately 30 cm in diameter and 50 cm high were extracted. In each core four circular planes of 16 electrodes each were fitted to the boundary walls. Having created steady-state upward vertical flow through the soil core, a salt tracer was injected in the base of the core and ERT measurements taken during and after injection of the tracer. For this experiment 2D ERT data were taken; that is, measurements were taken on each of the four horizontal planes. Because of the likely rapid development of flow pathways, Binley et al. (1996) used a high-speed data acquisition system designed for small scale industrial process monitoring. This system permitted data collection at a rate of 200 measurements per minute. Approximately 300 frames of data (including reciprocals) were collected for each plane for the duration of the experiment that lasted approximately 200 hours.

Figure 12 shows sample tomograms of one of the four image planes at selected times, relative to the background (pretracer injection) conditions. The results show the migration of the electrically conductive tracer through the core at this plane, and that the permeable (connected) pore space is significantly different from the impermeable bulk porosity (approximately 45%) with distinct zones showing rapid increase during injection and rapid recession after tracer injection ceased.

These core scale studies have been further developed to image 3D core volumes, as reported in Olsen et al. (1999), who also attempt to use changes in voxel properties to quantify solute transport model parameters. Such linkage between geophysical imaging and hydrological modeling is ongoing (see for example, Slater et al., 2000).

Mapping moisture migration in fractured tuff at the large block test

The Large Block Test (LBT) was a multidisciplinary field scale experiment performed by researchers from Lawrence Livermore National Laboratory with other laboratory and university collaborators, wherein a 3 × 3 × 4.5 m block of rock was studied as it was heated from ambient temperatures to approximately 145°C. The purpose of the test was to study coupled thermal, hydrological, chemical, and mechanical processes in response to heating at a scale significantly larger than what was possible in laboratory studies. Detailed descriptions of the test design, instrumentation, results and interpretation, and relevance to the nuclear waste isolation program can be found in numerous reports (e.g., Wilder et al., 1997; Lin et al., 1998).

A monolithic block of densely welded tuff was excavated from a site on Fran Ridge near Yucca Mountain, Nevada, so that coupled thermo-hydrological processes could be studied in a controlled, in-situ experiment. A series of heaters were placed in a horizontal plane about

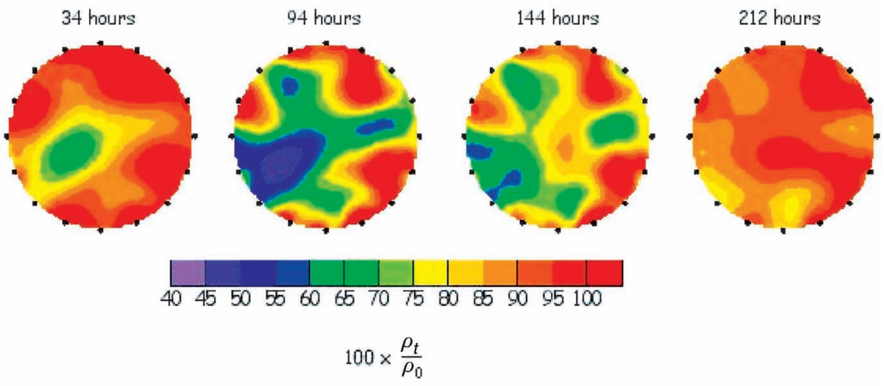

Figure 12. Selected 2D ERT tomograms showing change in resistivity across a horizontal plane of a soil core (after Binley et al., 1996). The circular plane is 32 cm in diameter and 28 cm from the position of a saline tracer source. The plane is surrounded by 16 electrodes (as shown). The tracer was injected between $t = 0$ and 97 hours.

3 m below the top of the 4.5 m high block. Temperatures were measured at many points within and on the block surface, and a suite of other measurements was taken to define the thermal and hydrologic response. Electrical resistance tomography was used to map 2D images of moisture content changes along four planes in the block.

Interpretation of ERT resistivity images in terms of moisture content is possible by using laboratory data establishing the relations between moisture, temperature, and resistivity, or by using a suitable petrophysical model of electrical conduction in porous media. Roberts and Lin (1997) have published data on the resistivity of Topopah Spring tuff as a function of moisture content. Ramirez and Daily (2001) combine these approaches and compare the saturations obtained using a petrophysical model with those using an activation energy relationship calibrated with laboratory data. Both approaches were compared with observed neutron probe estimates of moisture content during the test.

Waxman and Thomas (1974a,b) describe a model for electrical conduction in partially saturated shaly sands typical of oil reservoirs (intended for oil field data) which accounts for conduction through the bulk pore water as well as conduction through the electrical double layer near the pore surface. It can be shown that their model can be reduced to two bounding models: a model where the electrical double layer is the primary conduction pathway, and a model where the primary conduction pathway is through the pore-space volume (Ramirez and Daily, 2001). Temperature data were interpolated to construct temperature maps along each ERT image plane, and these maps were used to account for the effects of temperature on the measured resistivities. Calculation of changes in volumetric water content requires rock porosity and initial saturation values. Based on neutron log data, a uniform initial saturation of 75% and a porosity of 12% were assumed. The petrophysical model used to convert resistivity change to saturation assumes that the primary conduction pathway is through the pore-space volume.

Figure 13 compares changes in the volumetric water content inferred from ERT measurements with those inferred from the neutron probe data. The five black circles on the lower third of the image indicate the location of the heaters; also shown is the location of the borehole used for the neutron log comparison.

The main feature in both data (ERT and neutron probe) is the development of a large drying zone around the heater that grows from 1 m to 2 m thick in six months. Notice that from both of these measurements a maximum change in water content near the heaters is calculated to be about –0.07 volume percent. This close agreement is significant since the neutron log and ERT are two completely independent measurements. Another pronounced feature is the large change in resistivity in the upper left in the image. A time-lapse sequence of tomographs in Ramirez and Daily (2000) indicates that this feature gradually develops and persists throughout the duration of the test and is suggestive of a communicative fracture or fracture network that has allowed moisture to escape with subsequent dry-out of the adjacent matrix. There are also examples of compact anomalies of wetting. Some of these appear to be water accumulation in fractures that drain condensate from the block. Others may be due to rain water entering a fracture at the top of the block.

A second approach that can be used to estimate saturation from electrical measurements is based on the work of Roberts (2001). He discovered that laboratory measurements of welded tuff resistivity, taken as a function of temperature and saturation, can be represented using an Arrhenius relationship (see Roberts, 2001) connecting activation energy and temperature to electrical conductivity. We will compare this approach to the bounding models derived from the Waxman-Thomas model.

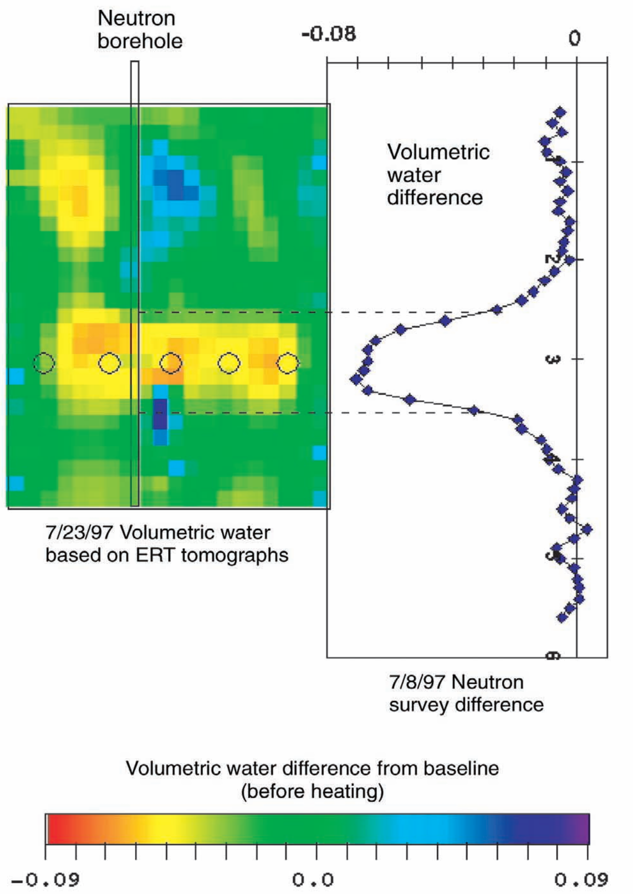

Figure 13. Comparison of changes in moisture content inferred from neutron logs and from ERT at the Large Block Test. The image plane is a 3 m (horizontal) by 4.5 m (vertical) 2D plane. The open circles indicate positions of the heater elements.

Figure 14 compares the saturations obtained using the three different approaches. The leftmost image was calculated using the Arrhenius equation method, calibrated with laboratory measurements of electrical properties versus temperature and saturation. The center and rightmost images were calculated using the two bounding models (based on the Waxman-Thomas model): a model where the electrical double layer is the primary conduction pathway, and a model where the primary conduction pathway is through the pore-space volume. A comparison of these three images indicates that the rightmost image (surface conductance dominant) shows the driest conditions near the vicinity of the heaters and the wettest conditions above the heater. Large regions of the block above the heaters are above 100% saturation (nonphysical). The left image (Arrhenius equation) shows less drying and less wetting than the other two. In particular, it shows that the wet regions at the top of the block reach 100% saturation and seldom exceed that value. Also, it shows that the dry region around the heaters has a saturation of approximately 15%, which compares favorably with saturation based on neutron data (approximately 10%). These results lead us to conclude that, of the three methods considered, the Arrhenius equation approach yields the most reliable estimate of saturation change for this particular example. The results also indicate that inference of hydraulic properties, in this case changes of water saturation, using ERT imaging is possible. However, the method is subject to several uncertainties that point to a need for improved petrophysical models relating electrical properties and moisture content.

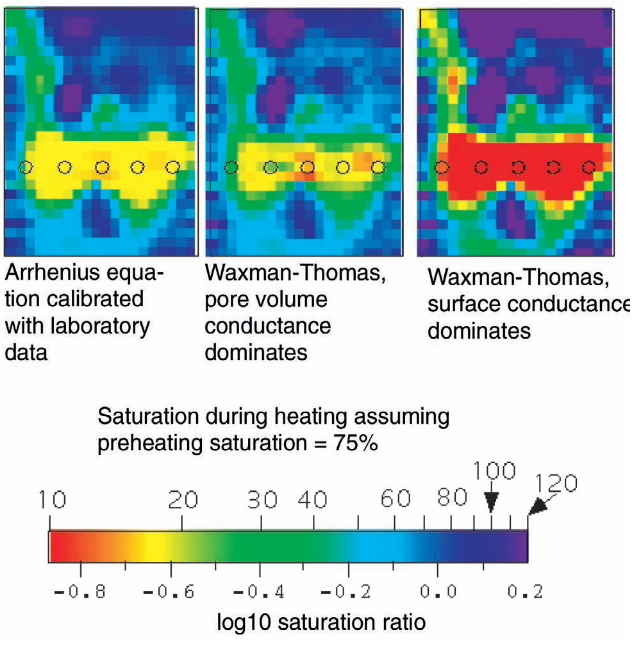
Arrhenius equation calibrated with laboratory data

Waxman-Thomas, pore volume conductance dominates

Waxman-Thomas, surface conductance dominates

Figure 14. Comparison of three different methods for calculating moisture content changes from resistivity changes.

ERT imaging in fractured media

Characterization of fractured rock and transport processes in fractured media is a necessary prerequisite to many environmental investigations. Because of the high contrasts in resistivity likely to exist in such dual porosity media, ERT may offer useful insight into the nature, extent, and connectivity of fracturing. However, because of the limited spatial resolution of ERT it is unreasonable to expect detection of individual fractures unless they are relatively large features. Slater et al. (1997b) have shown that the effects of networks of small fractures may be resolved using cross-borehole ERT imaging in chalk. In this work, saline tracers were injected in the vadose zone and the changes in electrical resistivity monitored over time. Slater et al. (1997b) conclude that they were unable to detect solute transport in the fractures, but were able to observe the effect of such transport, probably as a result of diffusion into the low permeability matrix.

In contrast, Slater et al. (1997a), in a study of a fractured carboniferous limestone, were able to identify a single fracture feature extending over tens of meters from cross-borehole ERT images. Figure 15a is an example of imaging capabilities in this environment. Using borehole televiewers, the cavities were observed to be several centimeters wide. Because of the high contrast in porosity, ERT is able to resolve a “feature” corresponding to the main fracture, but offers poor spatial resolution. Note also the borehole effects resulting from the use of electrode arrays in water filled (i.e., electrically conductive) open boreholes.

Slater et al. (1997a) studied the changes in ERT images following a large scale pumping test, carried out to investigate the local impact of dewatering to lower the floor level of an active quarry. This pumping test involved abstracting approximately 6500 l/hr from a trial excavation for a period of three weeks. The pumping created increases in local fluid conductivity by a factor of three due to the coastal proximity of the site. Slater et al. (1997a) were able to demonstrate that the fracture features observed from background imaging (as in Figure 15b) were hydraulically active since significant changes in ERT tomograms were observed. These results proved useful in assessing which units in the limestone are hydraulically significant and helped formulate a comprehensive environmental statement about the likely impact of quarry floor lowering at this site.

Practical application of ERT

The case histories we have discussed are typical examples of ERT results. The examples chosen represent work that was generally successful, but we recognize that there have been failures as well. This admission suggests the question: what makes the difference between success and

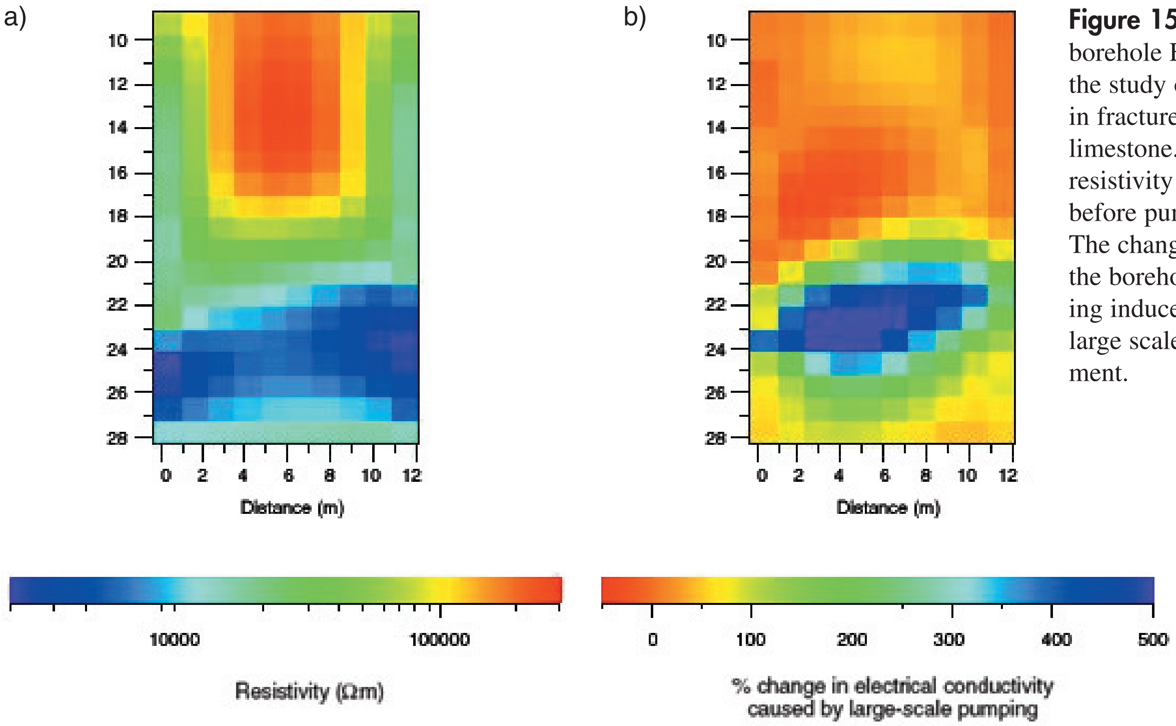

Figure 15. Example cross-borehole ERT image from the study of Slater (1997b) in fractured carboniferous limestone. (a) Baseline resistivity distribution before pumping began. (b) The change in resistivity in the borehole plane following induced salinity from a large scale pumping experiment.

failure? Of course, this question does not have a single answer. However, the answers are important, for knowing them could make the difference between success and failure with ERT. We list here some guiding principles that will help increase the probability of success with ERT:

- The ERT inverse process is inherently underdetermined so that more data is better than less data, provided the errors are known (see point 2). It is important that the data are internally consistent (e.g., the target's resistivity is stable during a measurement sequence—particularly relevant for process monitoring applications) and complete (contains all the linearly independent combinations).
- It is better to know the errors in the data than to have lots of data with uncertain errors. This rule is counterintuitive but it is true that a good measure of data errors is needed, because most of the inverse methods rely on statistical criteria to stop the inverse process when convergence is achieved. Without a noise estimate, the algorithms either end prematurely without using all the information in the data or end too late and spend iterations fitting the forward model to the data noise. In short, it is very important to know when to stop (demonstrated by Binley et al., 1995 and LaBrecque et al., 1996). Our experience leads us to believe that it is more important to spend valuable field time collecting the reciprocal for each measurement than collecting more dependent data. Forcing a model to fit measured data to 1% that has errors of 10% will result in tomographs that show unrealistic roughness—the reconstruction will have regions that look like a checkerboard.
- A comparison of repeated measurements, despite this being a very popular approach, will not produce a good measure of data errors. In fact, some very common sources or measurement errors (such as ground loops, electrode polarization, and amplifier saturation) can be extremely repeatable and completely missed by this test. All of our experience has convinced us that the best method of estimating error is to compare two reciprocal measurements. This method is sensitive to errors from electrode noise, electronic noise, grounding problems, common mode measurement problems, and any nonlinear effects in measurement system or subsurface.
- The need for an accurate forward solver is obvious; however, the problems from inaccurate forward solutions can be subtle and create artifacts. Some conditions that can lead to problems include 3D structures being modeled by a 2D forward model (e.g., a highly conductive annulus of grout around a borehole electrode array, as demonstrated in Figure 15a), differences between the actual electrode location and the modeled location, resistivity anisotropy, unknown or uncertain boundary conditions, and a mesh that is too coarse to accurately calculate the potentials near electrodes where high gradients exist.
- There is no strong evidence that a particular measurement scheme is superior. Several schemes have been used and compared, but it is likely that other factors dominate the reconstruction quality. On the other hand, there is good evidence that it is desirable to completely sample the image volume. A simple rule to achieve this is to distribute as many measurement electrodes as possible, as uniformly as possible through the volume. If

sampling is constrained to the perimeter of the image volume, it is best to completely surround the region of interest with electrodes. Of course, practical constraints usually limit electrode placement.

- A variety of experimental problems can degrade image quality. A common one is high electrode contact resistance resulting from installing electrodes in a borehole and filling the hole with dry sand. The ideal material will match the native soil conductivity. A good borehole completion material is native soil (it usually has some fines resulting in higher conductivity) or grout. A related problem can be caused by using highly conducting grout to cement an array in a highly resistive formation. When processed using a 2D algorithm, the electrical contrast will cause a resistive artifact along each borehole array that can only be removed by properly accounting for the grout anomaly in the model.
- Because ERT requires high-speed data collection on a large array of electrodes, the ideal electrode is inexpensive, rugged, long lasting, nontoxic, and electrically quiet (nonpolarizing). This last requirement means that an electrode can be used to measure a potential soon after it has been used to transmit a current (Dahlin, 2000). Tests to assess an acceptable delay time prior to full data collection are invaluable. A popular electrode material is stainless steel, but copper, iron, or steel are also good. Noisy electrodes are galvanized steel and aluminum. For surface arrays, the best data (good reciprocals for both magnitude and phase) can be obtained from nonpolarizing copper-copper sulfate electrodes (from our experience they can be used as current sources as well as potential electrodes).
- Care must be taken to avoid electromagnetic effects that violate the electrostatic approximation made in the forward model. For example, common electromagnetic coupling, which occurs when inductive currents become important compared to galvanic currents, can be avoided by keeping the induction number $\mu_0 \omega \sigma L^2$ small, where L is the characteristic length, ω is the angular frequency and σ is an effective conductivity.

Summary and Conclusions

Often several geophysical methods are used together, each lending its strengths to the problem at hand. We believe that electrical tomography will be used increasingly in this mode as it has some unique capabilities to offer the geophysicist. Of course, the method has limitations. We list here some of the strengths and weakness of ERT to help put the method in geophysical perspective. First the strengths:

- Because it is not necessary to move the sensors, ERT can be easily automated. Multiplexing of electrodes into an array of voltmeters, control of electronics, data storage and transmittal, and even data processing to a reconstructed image are all easily accomplished automatically under computer control. In fact, various parts of this automation have already been accomplished for long term monitoring of steam injection (see Ramirez et al., 1993). A data collection system has even been built to work remotely—it can be called up over a phone line, acquisition parameters set, acquisition started, data downloaded to a remote computer, and the system shut down. Automated or remotely controlled operation of ERT is ideal for long term (monitoring) and unmanned (and low cost) operation.
- Automatic data acquisition also promises the advantage of high-speed operation. The rate at which data can be acquired is a function of many conditions such as the frequency and staking, but typical acquisition rates at 1 Hz for commercially available systems can be as high as 2000 measurements per hour. High-speed acquisition can be more than a time saving convenience. For example, it can be critical when monitoring a rapidly evolving subsurface process such as a steam flood (LaBrecque and Yang, 2000) so that the data are self-consistent (all the data represent the same system state).
- Recent developments in computer technology as well as inversion algorithms have made for fast ERT data processing. Of course, improved computer technology encourages the solution of larger and more complex problems using larger and more complex software. The fact remains, however, that significant 3D inverse problems can now be routinely handled in a matter of hours. This, coupled with high-speed data acquisition makes real-time ERT for process control practical, as discussed earlier in the Visalia steam flood case study.
- Commercial data acquisition systems are now available at reasonable costs making ERT within the reach of universities and small geophysical service companies. Of course, more expensive equipment is also available for those needing more power and flexibility. Combined with the fact that ERT data processing algorithms are more sophisticated and robust, ERT is becoming widely available, in much the same way that ground penetrating radar matured over the past three decades.
- ERT imaging of galvanic electrical properties is a good complement to other geophysical methods. Resistivity is especially sensitive to porosity, pore connectivity, and conducting porefluid content. It is therefore a good complement to seismic velocity measurements that are very sensitive to lithology type and overburden pressure. Galvanic currents are also sensitive to the presence of fines and clays through surface electrochemistry effects (Marshall and Madden, 1959; Telford et al., 1976).

ERT also has limitations:

- At the low frequencies required for the electrostatic approximation, physical contact is required with the ground. Several schemes have been used for accomplishing this (grouting electrodes in boreholes, burying metal stakes at the surface, dragging metal electrodes over the surface for quick profiling [Christensen and Soensen, 1996]), but this requirement makes ERT impractical as a method for large-scale reconnaissance.
- Data processing codes have become increasingly more sophisticated and are now implementing several different algorithms. However, the inverse problem is intrinsically ill-posed and nonunique. For those unaware of the pitfalls, nonphysical (and absurd) results are common. Some training and experience are necessary to be consistently successful with current tools.
- Tomography requires interrogating the target from as many "views" as possible. Geophysical tomography, therefore, often requires drilling or pushing boreholes which are expensive and invasive. In many geophysical applications, it is impossible to sample the target satisfactorily (e.g., surround the image volume with electrodes) which results in reduced sensitivity and resolution.
- Probably the most disappointing attribute of ERT is its low spatial resolution, particularly when it is compared with X-ray tomography. It has been the observation of the authors that improvements in data density and accuracy have produced only modest improvement in spatial resolution.

Unlike ground penetrating radar or controlled source electromagnetic sounding, ERT is a relatively new technology. As a result, off the shelf hardware and robust software are not readily available so that user experience is still important for successful results. However, many groups, with both private and public support, are working to make ERT more user friendly and more widely available. Even so, as the case histories reported herein testify, considerable progress has been made. It is noteworthy, however, that twenty-four years ago Lytle and Dines (1978) stated research and development goals for ERT that are relevant even today. They noted in their pioneering paper on the *impedance camera*,

> Items worthy of future research include an assessment of the influence of noise in the data, a study of the accuracy of the reconstruction and its spatial dependence, an evaluation of the degree of dependence of various measurement configurations, an analytic study of the resolution limit, and a determination of the extent to which the use of a priori knowledge affects the interpretation.

Many of these items are still the subject of research.

Acknowledgments

The authors acknowledge the following for contributions to the case histories reported: Zonge Engineering and Research Organization, Tucson Arizona; Steamtech, Bakersfield, California; the Yucca Mountain Project, Las Vegas, Nevada; U. S. Navy, Mare Island, California. Jane Beatty, Mike Buettner, John Carbino, Wunan Lin, Siobhan Henry-Poulter, Robin Newmark, Dave Ruddle, and Lee Slater contributed to the success of many of the field projects. Richard Carlson was responsible for the LBT neutron data collection and analysis. We also acknowledge the contribution made by Andreas Kemna in the theoretical development of complex resistivity imaging.

The early research and development of ERT as a geophysical tool was funded by the U. S. Department of Energy and the Office of Civilian Radioactive Waste Management.

References

Alumbaugh, D. L., and G. A. Newman, 2000, Image appraisal for 2-D and 3-D electromagnetic inversion: Geophysics, **65**, 1455–1467.

Aki, K., A. Christoffersson and E. S. Husebye, 1976, Determination of the three-dimentional seismic structure of the lithosphere: Journal of Geophysical Research, **82**, 277–296.

Aki, K., and P. Richards, 1980, Quantitative seismology: Theory and methods: Freeman Press.

Anderson, D. L., and A. M. Dziewonski, 1984, Seismic tomography: Scientific American, **60**, 251.

Barber, D. C., B. H. Brown, and I. L. Freeston, 1983, Imaging spatial distributions of resistivity using applied potential tomography: Electronics Letters, **19**, 933–935.

Binley, A., A. Ramirez, and W. Daily, 1995, Regularised image reconstruction of noisy electrical resistance tomography data, *in* M. S. Beck, B. S. Hoyle, M. A. Morris, R. C. Waterfall, and R. A. Williams, eds., Process tomography: Proceedings, 4th Workshop of the European Concerted Action on Process Tomography, 401–410.

Binley, A., S. Henry-Poulter, and B. Shaw, 1996, Examination of solute transport in an undisturbed soil column using electrical resistance tomography: Water Resources Research, **32**, 763–769.

Binley, A., et al., 2001a, High resolution of vadose zone dynamics using cross-borehole radar: Water Resources Research, **37**, 2639–2652.

Binley, A., P. Winship, M. Pokar, and J. West, 2001b, Cross-borehole radar and resistivity tomography: A comparison of techniques in unsaturated sandstone, *in* Proceedings of the symposium on applications of geophysics to engineering and environmental problems

(SAGEEP2001): Environmental and Engineering Geophysical Society.

Bing, Z., and S. A. Greenhalgh, 2000, Cross-hole resistivity tomography using different electrode configurations: Geophysical Prospecting, **48**, 887–912.

Brown, B. H., and A. D. Seagar, 1985, Applied potential tomography—Data collection problems, *in* International conference on electric and magnetic fields in medicine and biology: IEE, 79–82.

Carlson, N. R., C. M. Mayerle, and K. Zonge, 1999, Extremely fast IP used to delineate buried landfills: 5th Meeting of Environmental and Engineering Geophysics—European Section, Expanded Abstracts, September 6–9.

Coggon, J. H., 1971, Electromagnetic and electrical modeling by the finite element method: Geophysics, **36**, 132–155.

Considine, D. M., 1983, Van Nostrand's scientific encyclopedia, sixth edition: Van Nostrand Reinhold Inc.

Christensen, N. B., and K. Sorensen, 1996, Pulled array continuous vertical electrical sounding (PA-CVES) with an additional inductive source, *in* R. S. Bell, and M. H. Cramer, eds., Proceedings of the symposium on applications of geophysics to engineering and environmental problems, Environmental and Engineering Geophysical Society, 1–10.

Dahlin, T., 2000, Short note on electrode charge-up effects in DC resistivity data acquisition using multi-electrode arrays: Geophysical Prospecting, **48**, 181–187.

Daily, W., and J. Lytle, 1983, Geophysical tomography: Journal of Geomagnetism and Geoelectricity, **35**, 423–442.

Daily, W. D., W. Lin, and T. Buscheck, 1987, Hydrological properties of Topopah Spring tuff: Laboratory measurements: Journal of Geophysical Research, **92**, 7854–7864.

Daily, W., and E. Owen, 1991, Cross borehole resistivity tomography: Geophysics, **56**, 1228–1235.

Daily, W., A. Ramirez, D. LaBrecque, and J. Nitao, 1992, Electrical resistivity tomography of vadose water movement: Water Resources Research, **28**, 1429– 1442.

Daily, W., A. Ramirez, R. Newmark, and V. George, 2000, Imaging UXO using electrical impedance tomography: Journal of Environmental and Engineering Geophysics, **5**, 11–23.

Daily, W., A. Ramirez, and K. Zonge, 1996, A unique data acquisition system for electrical resistance tomography, *in* Proceedings of the Symposium for the Applications of Geophysics to Environmental and Engineering Problems, SAGEEP'96.

deGroot-Hedlin, C., and Constable, S. C., 1990, Occam's inversion to generate smooth, two-dimensional models from magnetotelluric data: Geophysics, **55**, 1613–1624.

Dey, A., and H. F. Morrison, 1979a, Resistivity modeling for arbitrary shaped three-dimensional structure: Geophysics, **44**, 753–780.

Dey, A., and H. F. Morrison, 1979b, Resistivity modeling for arbitrarily shaped two-dimensional structures: Geophysical Prospecting, **27**, 106–136.

Dines, K. A., and R. J. Lytle, 1979, Computerized geophysical tomography: Proceedings of the IEEE, **67**, 1065–1073.

Ellis, R. G., and D. W. Oldenburg, 1994, The pole-pole 3D DC resistivity inverse problem: A conjugate gradient approach: Geophysical Journal International, **119**, 111–119.

Gisser, D., D. Isaacson, and J. C. Newell, 1987, Current topics in impedance imaging: Clinical Physics and Physiological Measurement, **8**, Supplement A, 39–46.

Geselowitz, D. B., 1971, An application of electrocardiographic lead theory to impedance plethysmography: IEEE Transactions on Biomedical Engineering, **BME-18**, 38–41.

Goble, J., and D. Isaacson, 1989, Optimal current patterns for three-dimensional electric current computed tomography: Proceedings of the Annual International Conference of IEEE Engineering in Medicine and Biology Society, **11**, 463–464.

Hestenes, M. R., 1980, Conjugate direction methods in optimization: Springer-Verlag Inc.

Hohmann, G. W., 1975, Three-dimensional induced-polarization and electromagnetic modeling: Geophysics, **40**, 309–324. (Errata in GEO-50-11-2279)

Hounsfield, G. N., 1973, Computerized transverse axial scanning (tomography): Part I. Description of system: British Journal of Radiology, **46**, 1016–1022.

Hubbard, S. S., et al., 1997, Estimation of permeable pathways and water content using tomographic radar data: The Leading Edge, 1623–1628.

Jackson, D. D., 1972, Interpretation of inaccurate, insufficient and inconsistent data: Geophysical Journal of the Royal Astronomical Society, **28**, 97–100.

Keller, G. V., and F. C. Frischknecht, 1966, Electrical methods in geophysical prospecting: Pergamon Press.

Kemna, A., 2000, Tomographic inversion of complex resistivity—Theory and application: Ph.D. thesis, Bochum University.

Kemna, A., and Binley, A. M., 1996, Complex electrical resistivity tomography for contaminant plume delineation: Proceedings of the 2nd Meeting of the Environmental and Engineering Geophysics Society, European Section, 196–199.

Kemna, A., A. Binley, A. Ramirez, and W. Daily, 2000, Complex resistivity tomography for environmental applications: Chemical Engineering Journal, **77**, 11–18.

LaBrecque, D. J., 1991, IP tomography: 61st Annual International Meeting of the Society of Exploration Geophysics, 413–416.

LaBrecque, D. J., and S. H. Ward, 1990, Two-dimensional cross-borehole resistivity model fitting, *in* S. H. Ward, ed., Geotechnical and environmental geophysics: Society of Exploration Geophysics, **3**, 51–74.

LaBrecque, D. J., G. Morelli, A. Ramirez, W. Daily, and P. Lundegard, 1995, Occam's inversion of 3D ERT data: Proceedings of the International Symposium on Three-Dimensional Electromagnetics 1995, Ridgefield, CT, 471–477.

LaBrecque, D. J., et al., 1996, The effects of noise on Occam's inversion of resistivity tomography data: Geophysics, **61**, 538–548.

LaBrecque, D. J., and X. Yang, 2000, Difference inversion of ERT data: A fast inversion method for 3D in-situ monitoring, *in* Proceedings of the Symposium on the Application of Geophysics to Engineering and Environmental Problems, Environmental and Engineering Geophysical Society, 907–914.

Lager, D. L., and R. J. Lytle, 1977, Determining a subsurface electromagnetic profile from high-frequency measurements by applying reconstruction-technique algorithms: Radio Science, **12**, 249–260.

Lesur, V., M. Cuer, and A. Straub, 1999, 2D and 3D interpretation of electrical tomography measurements, part 2: The inverse problem: Geophysics, **64**, 396–402.

Li, Y., and D. W. Oldenburg, 2000, 3D inversion of induced polarization data: Geophysics, **65**, 1931–1945.

Lin, W., et al., 1998, An overview of progress on the large block test: International High Level Waste Conference, Rep. UCRL-JC-128796, Lawrence Livermore National Laboratory.

Loke, M. H., and R. D. Barker, 1995, Rapid least-squares inversion of apparent resistivity pseudosections by a quasi-Newton method: Geophysical Prospecting, **44**, 131–152.

Lowry, T., M. B. Allen, and P. N. Shive, 1989, Singularity removal: A refinement of resistivity modeling techniques: Geophysics, **54**, 766–774.

Lundegard, P. D., and D. J. LaBrecque, 1995, Air sparging in a sandy aquifer (Florence, Oregon): Actual and apparent radius of influence: Journal of Contaminant Hydrology, **19**, 1–27.

Lytle, R. J., and K. A. Dines, 1978, An impedance camera: A system for determining the spatial variation of electrical conductivity: Lawrence Livermore National Laboratory UCRL-52413.

Marshall, D. J., and T. R. Madden, 1959, Induced polarization: A study of its causes: Geophysics, **24**, 790–816.

Morelli, G., and D. J. LaBrecque, 1996, Advances in ERT modeling: European Journal of Environmental Engineering and Geophysics, **1**, 171–186.

Oldenburg, D. W., and Y. Li, 1994, Inversion of induced polarization data: Geophysics, **59**, 1327–1341.

Oldenburg, D. W., and Y. Li, 1999, Estimating depth of investigation in DC resistivity and IP surveys: Geophysics, **64**, 403–416.

Olsen, P. A., A. Binley, S. Henry-Poulter, and W. Tych, 1999, Characterising solute transport in undisturbed soil cores using electrical and X-ray tomographic methods: Hydrological Processes, **13**, 211–221.

Park, S. K., and G. P. Van, 1991, Inversion of pole-pole data for 3D resistivity structure beneath arrays of electrodes: Geophysics, **56**, 951–960.

Ramirez, A., et al., 1993, Monitoring an underground steam injection process using electrical resistance tomography: Water Resources Research, **29**, 73–87.

Ramirez, A., W. Daily, and R. Newmark, 1995, Electrical resistance tomography for steam injection monitoring and process control: Journal of Environmental and Engineering Geophysics, **0**, 39–51.Ramirez, A., et al., 1996, Detection of leaks in underground storage tanks using electrical resistance methods, (Lawrence Livermore National Laboratory UCRL-JC-122180, October, 1995): Journal of Engineering and Environmental Geophysics, **1**, 189–203.

Ramirez, A., W. Daily, A. Binley, and D. LaBrecque, 1999, Electrical impedance tomography of known targets: Journal of Environmental and Engineering Geophysics, **4**, 11–26.

Ramirez, A., and W. Daily, 2001, Electrical imaging of the large block test—Yucca Mountain, Nevada: Journal of Applied Geophysics, **46**, 85–100.

Roberts, J., 2001, Electrical properties of Topopah Spring tuff as a function of saturation and temperature: Lawrence Livermore National Laboratory, UCRL-JC-142099.

Roberts, J., and W. Lin, 1997, Electrical properties of partially saturated Topopah Spring tuff: Water distribution as a function of saturation: Water Resources Research, **33**, 577–587.

Sasaki, Y., 1989, Two-dimensional joint inversion of magnetotelluric and dipole-dipole resistivity data: Geophysics, **54**, 254-262. (Discussion in GEO-54-9-1212-1212 with reply by author)

Sasaki, Y., 1994, 3D resistivity inversion using the finite-element method: Geophysics, **59**, 1839–1848.

Schima, S., D. J. LaBrecque, and P. D. Lundegard, 1996, Using resistivity tomography to monitor air sparging: Ground Water Monitoring and Remediation, **16**, 131–138.

Schlumberger, C., 1920, Etude de la prospection electrique du sous-sol: Gauthiers-Villars.

Shima, H., 1990, Two-dimensional automatic resistivity inversion technique using alpha centers: Geophysics, **55**, 682–694.

Shima, H., 1992, 2D and 3D resistivity image reconstruction using crosshole data: Geophysics, **57**, 1270–1281.

Shima, H., and T. Sakayama, 1987, Resistivity tomography: An approach to 2D resistivity inverse problems: 57th Annual International Meeting, SEG, Expanded Abstracts, Session: EM1.4.

Shore, G., 1992, E-SCAN resource mapping: Multidirectional electrical surveys: Premier Geophysics Inc.

Slater, L., A. Binley, and D. Brown, 1997a, Electrical imaging of the response of fractures to ground water salinity change: Ground Water, **35**, 436–442.

Slater, L., M. D. Zaidman, A. M. Binley and L. J. West, 1997b, Electrical imaging of saline tracer migration for the investigation of unsaturated zone transport mechanisms: Hydrology and Earth System Sciences, **1**, 291–302.

Slater, L., A. Binley, W. Daily, and R. Johnson, 2000, Cross-hole electrical imaging of a controlled saline tracer injection: Journal of Applied Geophysics, **44**, 85–102.

Tarantola, A., 1987, Inverse problem theory: Elsevier.

Telford, W. M., L. P. Geldart, R. E. Sheriff, and D. A. Keys, 1976, Applied Geophysics: Cambridge University Press.

Tikhonov, A. N., and V. Y. Arsenin, 1977, Solutions of ill-posed problems: W. H. Winston and Sons.

Tripp, A. C., G. W. Hohmann, and C. M. Swift, 1984, Two dimensional resistivity inversion: Geophysics, **49**, 1708–1717.

Van Voorhis, G. C., P. H. Nelson, and T. L. Drake, 1973, Complex resistivity spectra of porphyry copper mineralization: Geophysics, **38**, 49–60.

Vasco, D. W., A. Datta-Gupta, and J. C. S. Long, 1997, Resolution and uncertainty in hydrologic characterization: Water Resources Research, **33**, 379–397.

Wait, J. R., 1970, Electromagnetic waves in stratified media: Pergamon Press.

Waxman, M. H., and E. C. Thomas, 1974a, Electrical conductivities in shale sands—I. The relation between hydrocarbon saturation and resistivity index: Journal of Petroleum Technology (Feb.) 213–218; Transactions AIME, 257.

Waxman, M. H., and E. C. Thomas, 1974b, Electrical conductivities in shaly sands—II. The relation between hydrocarbon saturation and resistivity index; II. The temperature coefficient of electrical conductivity: Journal of Petroleum Technology (Feb.) 218–225; Transactions AIME, 257.

Webster, J. G. (editor), 1990, Electrical impedance tomography: Adam Hilger.

Wexler, A., B. Fry, and M. R. Neuman, 1985, Impedance-computed tomography algorithm and system: Applied Optics, **24**, 3985–3992.

Wilder, D., et al., 1997, Large block test status report, Lawrence Livermore National Laboratory, UCRL-ID-128776, August.

Wilt, M. J., et al., 1995, Crosswell electromagnetic tomography: System design considerations and field results: Geophysics, **60**, 871–885.

Yang, X., and D. J. LaBrecque, 1999, Stochastic inversion of 3D ERT data, *in* Proceedings of the Symposium on the Application of Geophysics to Engineering and Environmental Problems, Environmental and Engineering Geophysics Society, 221–228.

Yorkey, T. J., J. G. Webster, and W. J. Tompkins, 1885, Errors caused by contact impedance in impedance imaging, *in*, IEEE Seventh Annual Conference of the Engineering in Medicine and Biology Society, 632–637.

Yorkey, T. J., J. G. Webster and W. J. Tompkins, 1987, Comparing reconstruction algorithms for electrical impedance tomography: IEEE Transactions on Biomedical Engineering, **BME-34**, 843–852.

Zhang, J., R. L. Mackie, and T. Madden, 1995, 3D resistivity forward modeling and inversion using conjugate gradients: Geophysics, **60**, 1313–1325.

Zhao, S., and M. J. Yedlin, 1995, Some refinements on the finite difference method for 3D DC resistivity modeling: Geophysics, **61**, 1301–1307.

Zhou, B., and S. A. Greenhalgh, 1997, A synthetic study on cross-hole resistivity imaging with different electrode arrays: Exploration Geophysics, **28**, 1–5.